

Spatially Informed Independent Component Analysis for Oxygen-Enhanced MRI of the Human Lung

Sondre Elias Sigstad Wikberg

A dissertation submitted in partial fulfillment

of the requirements for the degree of

Master of Research

of

University College London.

Department of Medical Physics and Biomedical Engineering

University College London

August 15, 2025

I, Sondre Elias Sigstad Wikberg, confirm that the work presented in this thesis is my own. Where information has been derived from other sources, I confirm that this has been indicated in the work.

Abstract

This work develops an algorithm to use temporal ICA for robust estimation of a regionally varying gas-switching response during oxygen-enhanced MRI (OE-MRI) of the human lung. We apply the algorithm to a cohort of seven healthy- and ten long COVID subjects imaged with the same OE-MRI sequence. The estimated oxygen responses across manually segmented thoracic masks are used to fit piecewise exponential reference functions and statistically significant differences in the oxygen wash-in/wash-out parameters are found between cohorts. Furthermore, an average of $> 90\%$ of voxels are deemed oxygen-activated in either cohort, allowing spatially continuous and distributed estimation of oxygen wash-in, wash-out, and ventilation delay. By comparison, fitting models directly to the raw time series in each voxel in the thoracic mask yields activation percentages of $\sim 60\%$. Further work is needed to establish the clinical potential of the method and to render it computationally viable beyond the research setting.

Acknowledgements

I would like to acknowledge the help and support from my supervisors Dr. Mina Kim and Dr. Sarah Needleman. I would also like to thank my parents for their unwavering support throughout the work on this thesis.

Contents

1	Introduction and Background	15
1.1	Background	16
1.2	Existing Methods for Functional Lung Imaging	16
1.2.1	Computed Tomography (CT)	16
1.2.2	Nuclear Radiology	17
1.2.3	Magnetic Resonance Imaging (MRI)	18
1.3	OE-MRI	21
1.4	Dynamic OE MRI: Acquisition	21
1.4.1	Inversion Recovery at 1.5T	22
1.4.2	Direct and Simultaneous Acquisition of T_1 and T_2^* at 1.5T	22
1.4.3	OE-MRI at Low Field Strength	23
1.4.4	T_2^* Sensitised OE-MRI at 3T	23
1.4.5	Registration and Alignment	24
1.5	Estimation of the Dynamic Oxygen Effect	25
1.5.1	Direct Subtraction and PSE Maps	25
1.5.2	Pixelwise Curve Fitting	25
1.5.3	Independent component analysis (ICA)	27
1.5.4	Identifying Regionally Varying Response Times for OE-MRI	29
2	Independent Component Analysis	31
2.1	Outline of FastICA	31
2.1.1	Overview	31
2.1.2	Mathematical Formulation	32

	<i>Contents</i>	6
2.1.3	Independence and Independent Components	32
2.1.4	Ambiguities	33
2.1.5	Algorithm	34
2.2	Finding the Independent Components	36
2.2.1	Non-Gaussianity	36
2.2.2	Measures of Gaussianity	37
2.2.3	Uniqueness of the Solution	38
2.2.4	Why Maximise Non-Gaussianity	39
2.2.5	Iterative Maximisation of Negentropy	39
3	Spatially Averaged Temporal ICA for OE-MRI	44
3.1	Windowed ICA in the Literature	45
3.2	Theoretical Overview	45
3.2.1	The Sliding Window	45
3.2.2	Assumptions of the Method	47
3.3	Exploring the Parameter Space	48
3.3.1	Variation and The Number of Components	49
3.3.2	Initialising the ICA Algorithm	49
3.3.3	Identifying the oxygen-enhancement component	50
3.3.4	Grouping Voxels on Different Scales	51
3.3.5	Experiment Set-up & Computational Complexity	52
3.3.6	Experiment 1: Results	53
3.3.7	Experiment 1: Discussion	55
3.3.8	Combining Components	55
3.4	Algorithm	57
3.4.1	Reducing the Computational Burden for Multiple Scans . .	57
4	Modelling	61
4.1	Model Functions	61
4.2	Fitting	64
4.3	Testing for Differences Between Cohorts	65

<i>Contents</i>	7
4.4 Results	65
4.4.1 ICA weights	65
4.4.2 Model Distributions	68
4.4.3 Parameter Estimates	71
4.5 Discussion	75
5 General Conclusions and Future Work	78
Appendices	80
A Further Parameter Maps	80
Bibliography	84

List of Figures

- 1.1 From [1]: "[W]oman with suspected pulmonary embolism. A, Coronal dual-energy CT xenon map [...]. B, Coronal dual-energy CT iodine map [...]. C, Coronal maximum-intensity-projection pulmonary CT angiogram [...]." 17
- 1.2 From [2]: Coronal (top) and axial (bottom) SPECT scan measures of ventilation (left) and perfusion (right) in a patient with chronic thromboembolic hypertension. 18
- 1.3 From [3]: Hyper-polarised ^{129}Xe MRI of a healthy volunteer (left) and a subject with idiopathic pulmonary fibrosis (IPF, right). Rows show the gas-phase ventilation image (top, grey), the dissolved “barrier” signal from tissue–plasma (middle, green overlay) and the dissolved signal in RBCs (bottom, red overlay). 19
- 1.4 From [4]: Voxel-wise shift Δt_{CC} which maximises correlation of exponential function $r_4(t; \Delta t_{CC}) = S(t_i; R_{\text{enh}}, \tau_{\text{in}} = 30, \tau_{\text{out}} = 25, \Delta t_{CC})$ with raw timeseries of voxel, $(q_i)_{i \in [21, \dots, 60]}$ 27

1.5 From [5]: Two registered MRI images in different slices from the same subject. (B) Percent Signal Enhancement (PSE) maps generated using the (co-registered) raw time series of each voxel. (C) PSE maps using the extracted OE-component for each slice and the associated voxel-wise weights. For each voxel, a mean S_{air} of the raw signal during the initial period of air inhalation was calculated alongside an average S_{oxy} from the last 5 dynamics of each O_2 -delivery lobe. The PSE maps in (B) were then generated as $(S_{oxy} - S_{air})/S_{air}$. A corresponding ratio r_{OE} was calculated for the OE-component \mathbf{s}_{OE} shared by all voxels. The PSE maps in (C) were generated by calculating for each voxel i the product $a_{i,OE}r_{OE}$, where $\mathbf{a}_{:,OE}$ is the column-vector of mixing weights for \mathbf{s}_{OE} .	29
3.1 Top Left: Single dynamic from OE-MRI scan, Top Right: Manually segmented lung mask, Bottom Left: Sliding window (in white) with radius $r = 4$ at a particular location within lung mask. Note that the number of voxels in the window is not truncated as the window is sufficiently removed from the edges of the mask. Bottom Right: Sliding window with radius $r = 4$ at location along edge of mask. The number of voxels in the window gets truncated accordingly.	46
3.2 Fifteen reference functions are shown with transition to cyclic oscillations at some delay $n\Delta t$ after the first gas switch. For Scan 1, $t_1 = 90s$ and $\Delta t = 1.5s$. To avoid cluttering, further gas switches are not plotted, but in accordance with the shape of the reference functions, the first switch from O_2 to air would occur at a time Δt before the trough in the clear blue curve	51
3.3 Experiment 1 Statistics. Left: Median of best Spearman correlation extracted from each run of ICA against dimensionality c , stratified by window radius. Hashed areas show the 10-90th percent interval. Right: Corresponding plot showing ratio of first to second-best Spearman correlation from each run of ICA.	53

3.4 Experiment 1 Statistics. Left: In each window every dimensionality c receives a rank according to the best Spearman coefficient produced at with c dimensions. This plot is a rank-wise median of those scores over all window. Hashed areas show 10th and 90th percentiles of the rank-wise Spearman correlations. Right: The equivalent plot (in particular according to the same ranking) for the ratio of best to second-best Spearman correlation from each ICA run. The tails show spikes in the 10th and 90th percentile due to the limited number of runs in which all 13, 29 and 49 dimensionalities could be tested (corresponding to radii 2,3,4).	54
3.5 Statistics for Experiment 1. Each voxel a represents a property of the optimal component extracted in window $W(a; r)$ with radius r as indicated. Top: Dimensionality c leading to highest Spearman correlation; $\arg \max_c (\max_l \rho(1, l, c))$. Middle: Best Spearman correlation extracted in the window centred at each voxel; $\max_{l,c} \rho(1, l, c)$. Bottom: The stability to initialisation of the best Spearman coefficient across all dimensionalities; $\max_{l,c} \rho(1, l, c) - \min_l (\max_c \rho(1, l, c))$	56
3.6 Weights \bar{a}_v^2 in each voxel from Algorithm 3 applied to <i>Scan 1</i> first with $m = 60$, $\epsilon = 5$, $c_{\max} = \infty$ and then with $m = 3$, $\epsilon = 1$, $c_{\max} = 40$. For both runs $R = \{2, 3, 4\}$	59
3.7 Pearson correlation between estimated oxygen responses $\mathbf{o}_v^{(1)}$ and $\mathbf{o}_v^{(2)}$ as produced from Algorithm 3 applied to <i>Scan 1</i> first with $m = 60$, $\epsilon = 5$, $c_{\max} = \infty$ and then with $m = 3$, $\epsilon = 1$, $c_{\max} = 40$. For both runs $R = \{2, 3, 4\}$	60
4.1 Three examples of the most complex piecewise exponential function f_4 for $\theta = (0, 0.001, 1, \Delta t, 30, 20)$, $t_1 = 60$, $P = 120$, and different delays $\Delta t = 0, 10, 20$	63

4.2 Weights \bar{a}_v^2 in each voxel from Algorithm 3 applied to the healthy and long COVID cohorts, respectively. Note that all slices have been placed on the same intensity scale, which is the reason <i>Scan 1</i> (the last of the slices in the healthy cohort) appears slightly dim compared to Figure 3.6.	66
4.3 Mean empirical cumulative density function (ECDF) for the weights for the healthy and long COVID cohorts. Empirical CDFs are generated for each subject (using 100 bins) and then averaged at each weight level. The hashed areas show the standard error of the mean ECDF for each cohort. Vertical lines show the median weight for each cohort as estimated from the mean ECDF.	67
4.4 Proportion of voxels for which each model produced the best AICc score when fitted to the oxygen responses estimated by Algorithm 3, stratified by cohort. Bars correspond to the average proportion across scans, while the points correspond to proportions within individual scans.	68
4.5 Proportion of voxels for which each model produced the best AICc score when fitted to the raw (registered) time series, stratified by cohort. Bars correspond to the average proportion across scans, while the points correspond to proportions within individual scans. . .	69
4.6 Right: Mean ECDFs for wash-in parameter τ_{in} in oxygen-activated voxels as found with fits to the time series from Algorithm 3 Left: Equivalent plots for fits to raw time series. For both figures, 60 bins were used for the ECDF.	70
4.7 Right: Mean ECDFs for wash-out parameter τ_{out} in oxygen-activated voxels as found with fits to the time series from Algorithm 3 Left: Equivalent plots for fits to raw time series. For both figures, 60 bins were used for the ECDF.	70

4.8	Right: Mean ECDFs for delay parameter Δt in oxygen-activated voxels as found with fits to the time series from Algorithm 3 Left: Equivalent plots for fits to raw time series. For both figures, 60 bins were used for the ECDF.	70
4.9	Right: Mean ECDFs for oxygen response scale parameter ΔS in oxygen-activated voxels as found with fits to the time series from Algorithm 3 Left: Equivalent plots for fits to raw time series. For both figures, 120 bins were used for the ECDF.	71
4.10	Right: Mean ECDFs for coefficient of determination \bar{R}^2 when comparing estimated oxygen responses from ICA method with optimal fitted function (among $f_1 - f_6$). Left: Equivalent ECDFs estimated using raw time series. In both cases 120 bins were used to generate the ECDFs.	72
4.11	Fitted wash-in rate τ_{in} in third coronal slice for estimated oxygen responses from ICA Algorithm 3. Black pixels represent voxels where models f_5 or f_6 provided the best fit (i.e. not oxygen-activated).	73
4.12	Fitted wash-in rate τ_{in} in third coronal slice for raw time series. Black pixels represent voxels where models f_5 or f_6 provided the best fit (i.e. not oxygen-activated).	74
1	Fitted wash-out rate τ_{out} in third coronal slice for estimated oxygen responses from ICA Algorithm 3. Black pixels represent voxels where models f_5 or f_6 provided the best fit (i.e. not oxygen-activated).	80
2	Fitted wash-out rate τ_{out} in third coronal slice for raw time series. Black pixels represent voxels where models f_5 or f_6 provided the best fit (i.e. not oxygen-activated).	81
3	Fitted delay Δt in third coronal slice for estimated oxygen responses from ICA Algorithm 3. Black pixels represent voxels where models f_5 or f_6 provided the best fit (i.e. not oxygen-activated).	82

- 4 Fitted delay Δt in third coronal slice for estimated oxygen responses from ICA Algorithm 3. Black pixels represent voxels where models f_5 or f_6 provided the best fit (i.e. not oxygen-activated). 83

List of Tables

4.1	Initial values and optimisation bounds used in voxel-wise fitting	64
4.2	Bootstrapped confidence intervals for the difference $\mathbb{E}[\mu COVID] - \mathbb{E}[\mu Healthy]$ in cohort-wise mean of means of different parameters fitted on the estimated oxygen responses using the ICA model (Algorithm 3) and the raw time series. An asterisk denotes that we reject the null hypothesis of no significant difference at the 5% significance level.	72
4.3	Bootstrapped parameters CIs for $\mathbb{E}[\mu COVID] - \mathbb{E}[\mu Healthy]$ only in voxels deemed oxygen-activated when fitted using both the raw time series and the estimated oxygen responses using Algorithm 3. An asterisk denotes that we reject the null hypothesis of no significant difference at the 5% significance level.	75

Chapter 1

Introduction and Background

This project aims to use dynamic oxygen-enhanced magnetic resonance imaging (OE-MRI) to extract functional information about ventilation and perfusion of the human lung. While oxygen-enhanced MRI is a promising tool for functional lung imaging, extraction of the oxygen-enhancement signal remains challenging due to the low signal-to-noise ratio of lung MRI and confounding factors such as density changes due to respiration and heartbeat. Current methods characterise the nature of oxygen sensitivity by looking either at individual voxel time series in isolation or by extracting a shared "oxygen enhancement component" (OE component). The former method suffers from inevitable inaccuracies, as the time series of a single voxel is influenced by multiple confounding processes and is only weakly informative of the underlying oxygen response when considered in isolation. The latter method is able to remove some of these problems by looking at common patterns across all voxels, but is then unable to identify regional differences in the shape and timing of oxygen sensitivity. We aim here to propose and test a method for processing OE-MRI scans that strikes a balance between extracting common features and allowing regional variation in the identified oxygen response.

In the remainder of the present chapter, we will discuss existing methods for functional lung imaging and previous applications of OE-MRI for lung imaging. In chapter 2, we will outline the mathematics underlying independent component analysis. This will be an important stepping stone to the method for oxygen response estimation from OE-MRI developed in chapter 3. Finally, chapter 4 will fit refer-

ence functions for oxygen wash-in and wash-out to the estimated response across the lungs of a healthy and diseased cohort.

1.1 Background

Modern respiratory medicine increasingly recognises that many lung disorders – such as asthma, cystic fibrosis (CF), and chronic obstructive pulmonary disease (COPD) – are intrinsically *heterogeneous*, affecting different regions with varying severity and temporal progression. Metrics like spirometry, which is a global measure of ventilatory capacity, can remain within normal limits even as regional structure and function deteriorates [6]. Spatially resolved imaging such as computed tomography (CT), PET, and MRI can detect detailed structural- and sometimes functional outcomes of disease long before any change appears through spirometry. However, existing methods sometimes suffer from an inability to capture *dynamic* information about function and can be expensive and logically demanding [7]. Consequently, there is a pressing need for functional imaging techniques that deliver *dynamic, voxel-wise* biomarkers of ventilation, diffusion and perfusion while remaining safe, reproducible and feasible in routine practice.

1.2 Existing Methods for Functional Lung Imaging

Functional imaging of the lung is currently performed with a variety of x-ray, nuclear medicine, and electromagnetic techniques. These methods vary in the information they can provide on each step in the chain from gas delivery to blood uptake. Furthermore, different methods come with different levels of accuracy and risk, both of which must be taken into account when assessing their usefulness in a clinical setting.

1.2.1 Computed Tomography (CT)

CT reconstructs x-ray projections into two- or three-dimensional density maps, and regional ventilation can be inferred by non-rigidly registering inspiratory and expiratory image stacks to calculate local volume change from the Jacobian determinant [6]. CT can also be used in combination with the inhalation of heavy gases such as

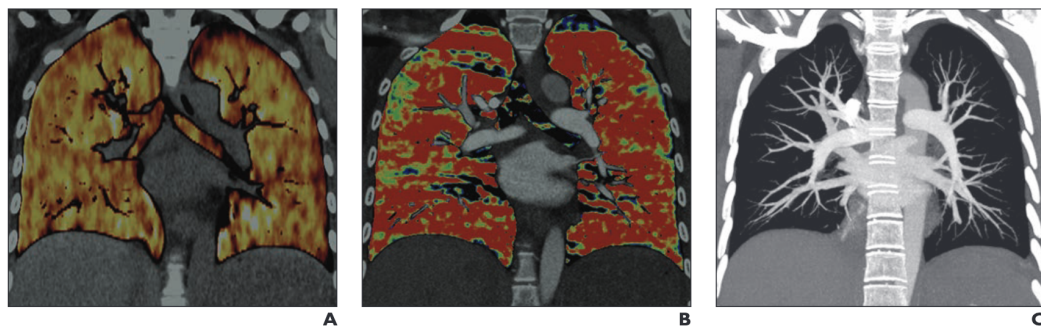


Figure 1.1: From [1]: "[W]oman with suspected pulmonary embolism. A, Coronal dual-energy CT xenon map [...]. B, Coronal dual-energy CT iodine map [...]. C, Coronal maximum-intensity-projection pulmonary CT angiogram [...]."

such as Xenon (Xe), which improve x-ray contrast and therefore enable direct measurement of regional wash-in and wash-out rates during dynamic image acquisition [8]. Dual energy CT (DECT) acquires two energy spectra simultaneously and, by material decomposition, isolates inhaled gases such as Xe and injected substances such as iodine to create voxel-wise ventilation and perfusion maps, respectively[8]. CT is ubiquitous, fast, and submillimeter in resolution, but it exposes patients to ionizing radiation and is comparatively invasive when dependent on inhalation of Xe or injection of iodine which can cause anesthetic and allergic reactions, respectively. These factors cause the method to have limited longitudinal, paediatric, and clinical use [2, 6]. However, the recent development of photon-counting CT reduces radiation exposure while improving image quality, making CT for functional lung imaging more attractive [2]. Figure 1.1 shows ventilation (A) and perfusion (B) maps as generated by a DECT scan during inhalation of 30% Xenon (70% oxygen) and injection of an iodine bolus [1].

1.2.2 Nuclear Radiology

Nuclear techniques for lung imaging function by detecting particles emitted by a radioactive tracer inhaled or injected to investigate ventilation and perfusion, respectively, in a subject [8]. As implied by the name, single-photon emission computed tomography (SPECT) uses tracers emitting a single photon during decay. The photon's line of travel must be determined approximately from the angle of incidence on a rotating detector. On the other hand, positron emission tomography (PET) uses

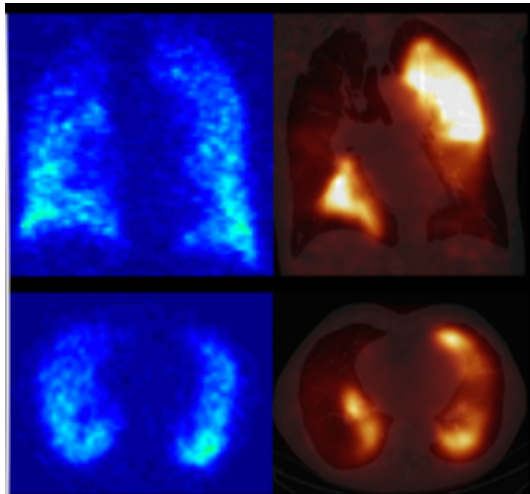


Figure 1.2: From [2]: Coronal (top) and axial (bottom) SPECT scan measures of ventilation (left) and perfusion (right) in a patient with chronic thromboembolic hypertension.

tracers emitting two photons traveling in opposite directions, allowing precise information about the line along which the decay occurred. Since, tracer densities are found by tomographic reconstruction, the accurate lines of travel in PET provide for millimetre-scale resolution, whereas SPECT has an optimal resolution of about 1cm.

PET and SPECT may be used for lung imaging to produce dynamic ventilation-perfusion maps, often labeled \dot{V}/\dot{Q} scans. \dot{V}/\dot{Q} scans can identify overlapping regions of high ventilation but poor perfusion, and are therefore used extensively to image patients with suspected pulmonary embolism [6]. Despite the finer resolution of PET, the radiation dose delivered by SPECT is significantly lower and tracers are longer-lived and more easily available. SPECT scans are more widely available in non-research settings [8]. Figure 1.2 illustrates coronal and axial maps of ventilation and perfusion in a patient with chronic thromboembolic hypertension.

1.2.3 Magnetic Resonance Imaging (MRI)

Magnetic resonance imaging (MRI) works by manipulating the magnetic field around a sample so that the magnetic moments of particles precess at position-dependent frequencies. By recording the resulting change in net magnetisation over

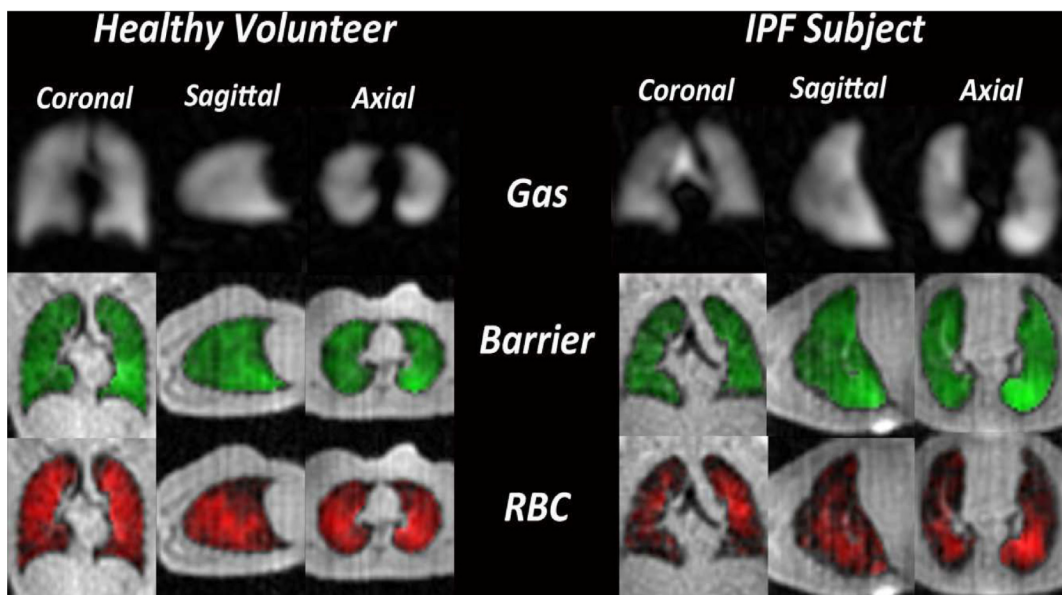


Figure 1.3: From [3]: Hyper-polarised ^{129}Xe MRI of a healthy volunteer (left) and a subject with idiopathic pulmonary fibrosis (IPF, right). Rows show the gas-phase ventilation image (top, grey), the dissolved “barrier” signal from tissue–plasma (middle, green overlay) and the dissolved signal in RBCs (bottom, red overlay).

time and applying an inverse Fourier transform, the particle density at each location is reconstructed. MRI, which is (practically) radiation-free, can interrogate lung function with several techniques [2].

Hyperpolarised noble gas MRI images inhaled ^{129}Xe or ^3He whose magnetisation has been boosted, enabling three-dimensional breathhold ventilation maps. Furthermore, Xe is soluble, with distinct chemical shifts depending on its state. Hence, the regional transfer of Xenon from gaseous state in the alveoli, through to interstitial tissue and red blood cell (RBC) compartments may be quantified [8]. Figure 1.3 shows the results of such a scan for a healthy and a diseased subject, respectively [3]. While hyperpolarised gas MRI can image gas presence directly, it requires expensive hardware for polarisation of gases and is limited to a handful of centres.

The particle most convenient to image on MRI of biological tissue is the single proton present in hydrogen (^1H), due to the abundance of hydrogen. However, in the lungs, the density of particles is much reduced relative to the surrounding tissue, which complicates the effort of using this MRI modality (“proton MRI”) to

extract functional information. Techniques such as arterial spin labelling (ASL) and dynamic contrast-enhanced MRI (DCE MRI) measure absolute perfusion by magnetically labelling blood water or tracking a high-density gadolinium bolus, respectively [2]. The labeled blood or gadolinium, which act much like tracers, change the magnetisation in perfused areas, thus being detectable on an MRI scan. DCE MRI for perfusion measurement is used routinely in clinical settings for "assessment of COPD, CF, and pulmonary vascular disease" [9]. Clinical use of ASL MRI has remained limited, however [2]. Both methods suffer from the need for additional equipment which must work in tandem with an MRI scanner, which may increase invasiveness and the logistical burden.

Contrast-free methods in proton MRI rely on the changing magnetic properties of the lung parenchyma (T_2^* reduction) and blood (T_1 reduction and inflow of particles not magnetised). (These phenomena will be discussed further in the next section.) Fourier-based methods rely on high sampling frequencies in time which are used to pick out distinct cardiac and respiratory frequencies during chest imaging. Dynamic information on ventilation and perfusion is then gathered from the spectral amplitude of these frequencies at different positions in the lung. One Fourier-based technique which has shown particular promise is phase-resolved functional lung MRI (PREFUL) [10]. This method works by capturing a series of images during free-breathing and determining the phase of each within respective cardiac and respiratory cycles. According to their phase, images are then reordered so that an even more fine-grained pseudo time-series of each cycle is produced. The fine temporal details of voxel-wise changes over each cycle allow dynamic estimates of ventilation and perfusion [10]. Proton-only methods are attractive as they allow free-breathing acquisitions and typically do not require additional physical equipment. However, advanced methods such as PREFUL depend to a large extent on the quality of co-registration of images and advanced post-processing which has remained a computational hurdle [2].

1.3 OE-MRI

Oxygen-enhanced ^1H magnetic resonance imaging (OE-MRI) of human lungs was first proposed by Edelman et al. in a 1996 article in Nature [11]. The method was developed in the wake of the emergence of BOLD imaging in the early 1990s, during which time it was discovered that ^1H MRI was sensitive to the differing magnetic properties of oxygenated and de-oxygenated hemoglobin. OE-MRI of the lung uses pure O_2 as an inhaled contrast agent which gets expressed by increased magnetic susceptibility gradients at the gas-tissue interface induced by pure gaseous O_2 in the alveoli (T_2^* reduction) *and* the paramagnetic property of dissolved O_2 in lung-tissue water and the pulmonary vasculature (T_1 reduction) [12, 5].

As originally proposed, the OE-MRI method has subjects breathing medical air and 100% O_2 through a non-rebreathing mask at intervals lasting up to several minutes, during which images are acquired. The promise of the model lies in analysing the changes to images generated as oxygen and medical air are cycled, to make inferences about the distribution and uptake of oxygen. From a clinical perspective, the method is highly attractive as 100% O_2 is readily available in most hospitals and carries few risk factors when inhaled over short periods of time.

Due to the extremely short T_2^* of the lung, most studies have focused on global estimation of T_1 changes during pure oxygen inhalation [12]. However, the drop in T_1 is driven chiefly by the rise in dissolved, paramagnetic O_2 that accompanies blood perfusion, whereas the shortening of T_2^* stems mainly from the stronger air-tissue susceptibility gradients that form around ventilated alveoli, thereby encoding ventilation information [5]. We are therefore interested in MRI sequences sensitive to changes in both parameters. Whereas the change in T_1 has often been evaluated by comparing cardiac- or respiratory-triggered images, recent studies have acquired images from the full respiratory cycle [5].

1.4 Dynamic OE MRI: Acquisition

Due to the minimal signal available from the lung parenchyma (due to low proton density) during proton-MRI and the artefacts associated with lung movement, the

timing and frequency of image acquisition during OE-MRI is highly relevant to the conclusions which may be drawn from an experiment. Several imaging sequences and modelling approaches have been used to estimate the static and dynamic changes to T_1 and T_2^* indicative of perfusion and ventilation. Here, we will summarise some of the acquisition schemes that have been proposed for OE-MRI of the human lung.

1.4.1 Inversion Recovery at 1.5T

A large corpus of work has used acquisition strategies targeting the oxygen-related T_1 shortening as measured by inversion recovery (IR) sequences at 1.5T. Edelman's original single-slice IR-HASTE images were acquired every three seconds over alternating medical air and pure oxygen delivery periods at 1.5T with total scanning lasting between two and four minutes. In a later paper by Mai *et. al.*, diastole-triggered acquisitions were used to improve comparability of images. The interleaved delivery periods of medical air and O_2 lasted approximately 3 minutes, respectively. This paper was also notable for its use of multiple inversion recovery-HASTE (MIR-HASTE) which nulled the magnetization of muscle and fat and therefore more clearly showed parenchymal tissue [13]. In these and other studies to 2008 using inversion recovery at 1.5T, signal enhancements were shown to be consistent with static T_1 shortening in manually chosen parenchymal regions of interest in the range of 6.7 – 13.7% [12].

1.4.2 Direct and Simultaneous Acquisition of T_1 and T_2^* at 1.5T

Triphan *et. al.* used a two-dimensional radial UTE sequence at 1.5T in which a single non-selective inversion pulse was followed by a train of ~ 300 low-flip gradient-echo spokes, each sampled at three echo times (0.07, 1.2, 2.3ms) so that multiple reads occurred within one inversion period [14]. The dense series of first-echo spokes tracks longitudinal recovery and allows voxel-wise estimation of T_1 , while the three echoes in every spoke capture transverse decay and permit simultaneous fitting of T_2^* . Uniform golden-angle rotation of the spokes yields motion-robust, inherently co-registered T_1 and T_2^* maps from a single free-breathing scan. However, the complexity of the acquisition sequence is a bottleneck and the

method has rarely been applied elsewhere.

1.4.3 OE-MRI at Low Field Strength

A review by Xu *et. al.* from 2023 emphasises that moving OE-MRI to “lower-field” scanners ($B_0 < 1.5\text{T}$, particularly new 0.55T platforms) lowers susceptibility gradients and therefore extends parenchymal T_2^* from $\sim 1.8\text{ ms}$ at 1.5T to $\sim 10\text{ms}$ at 0.55T , while simultaneously shortening T_1 ; together these effects raise the percent signal enhancement ($\text{PSE} \approx 19\% \pm 11\%$ at 0.55T vs. $7.6\% \pm 6.3\%$ at 1.5T) and permit fast, low-SAR sequences such as multi-slice IR-HASTE [12]. Early 0.2T permanent-magnet systems were limited by low SNR, but modern 0.55T superconducting units recover fine parenchymal detail at lower cost, leaving the main trade-off the need for more complex reconstruction to manage concomitant-field artefacts in 3-D non-Cartesian imaging.

1.4.4 T_2^* Sensitised OE-MRI at 3T

In a paper from 2024, Kim *et. al.* used a free-breathing dual-echo RF-spoiled gradient echo sequence at 3T , $\text{TR} = 16\text{ms}$ to directly estimate T_2^* -values in the lung parenchyma of 16 healthy volunteers during steady-state air and O_2 inhalation, respectively [15]. The temporal resolution was 1.54 s for six coronal slices. Combining the estimated difference ΔT_2^* with the corresponding ΔT_1 reported in the literature, they then simulated MRI signal differences ΔS between air and O_2 inhalation, with different values of flip angle and TE. They find that maximal absolute ΔS are found for flip angle = 5° (regardless of TE) and that for $TE > 0.2\text{ms}$, ΔS is primarily determined by ΔT_2^* rather than ΔT_1 . Absolute ΔS was maximised by $TE \in [0.5, 1.5]\text{ms}$. Successive echo times of $TE_1 = 0.71\text{ms}$ and $TE_2 = 1.2\text{ms}$ were the shortest possible on the machines used in the study. In simulation, the first echo at time $TE_1 = 0.71\text{ms}$ was shown to contain a small T_1 weighting, but simulations confirmed that ΔR_2^* accounted for the majority of measured percent signal enhancement. Therefore, the protocol was classified as T_2^* -*sensitised* [15].

1.4.5 Registration and Alignment

When attempting to capture the signal change induced by pure oxygen inhalation, the tissue movement induced by cardiac and pulmonary movement must be accounted for. Edelman determines from all images a most-common pixel position for the lung-diaphragm interface. Only air-oxygen pairs with this interface in the same position are subtracted and divided by the corresponding air-image to generate percentage enhancement maps accounting for the fact that baseline signal in the lung is low relative to surrounding tissue [11]. Such a method, however, only demands that the physiology is similar at a particular point, whereas a given pixel, elsewhere in the FOV, could represent different sections of tissue between two images.

Other authors have used cardiac or respiratory triggers to capture images of the lungs at a similar point in the respiratory-cardiac cycle. In such cases, the tissue type in each pixel is expected to be largely the same between images, and direct use of the images or averages (rolling or absolute) over the separate gas delivery schemes may be used to assess the effect of oxygen inhalation [13, 4, 16]. Dietrich *et. al.* kept the same IR-HASTE read-out but introduced *double triggering* (end-expiration and mid-diastole) to acquire 80 frames (air /O₂ /air /O₂) with minimal blurring [4]. However, cardiac or respiratory triggering used in isolation may still capture images with different physiology, as the unused factor is at a different point in its cycle. Additionally, these methods fail to account for potential patient movement.

Other authors have used image registration to force pixel-physiology alignment across images [17, 15, 5]. Such methods typically deform a domain such that a set of reference points remain within the same position. A benefit of this approach is that images from the full respiratory and cardiac cycle may be used. However, the registration process involves interpolation which may smear important tissue boundaries delineating widely different signal responses to oxygen.

Finally, Kim *et. al.* [15] use registration coupled with proton density correction to assess the median signal difference between inhalation of air and oxygen. The benefit of such an approach is that it accounts for density changes induced by O₂

inhalation, such as vasodilation, which may influence the measurement of intrinsic signal change. However, the sponge model used for this purpose accounts only for density changes induced by ventilation, and may therefore be inaccurate in regions heavily affected by perfusion [15].

1.5 Estimation of the Dynamic Oxygen Effect

1.5.1 Direct Subtraction and PSE Maps

Perhaps the simplest way with which to assess the effect of oxygen is, as in the original paper by Edelman [11], to subtract aligned/registered oxygen and air images, after which the result is divided by the air image. This produces a percentage signal enhancement (PSE) map demonstrating the proportion by which oxygen has modulated the signal in each pixel, relative to the "baseline" under air inhalation.

This method can conveniently be used to assess the effect of oxygen throughout the lung on average or at a particular manually selected region of interested [13]. However, such maps do not give global nor local information about the rates and timing of oxygen wash-in and wash-out, which are essential to assess phenomena such as delayed ventilation.

1.5.2 Pixelwise Curve Fitting

In 2001 work by Hatabu *et. al.* [18], global left- and right lung wash-in (τ_{in}) and wash-out (τ_{out}) rates of O_2 were estimated separately with an exponential model:

$$\begin{aligned} S_{\text{in}}(t) &= (A - B) \exp[-\tau_{\text{in}}(t - t_1)] + B & t_1 \text{ is time of switch to } O_2 \\ S_{\text{out}}(t) &= (A - B)(1 - \exp[-\tau_{\text{out}}(t - t_2)]) + B & t_2 \text{ is time of switch back to air,} \end{aligned}$$

where A, B denote the steady state values under air and O_2 inhalation respectively. The voxel intensities from images acquired every 3s during wash-in and wash-out were averaged across manually selected ROIs in the left and right lungs, respectively. The procedure was repeated for the scans of nine volunteers and wash-in/wash-out times were estimated as (26.8, 23.3) and (26.3, 20.8) in the right and left lungs, respectively.

In [17], image co-registration was combined with voxel-wise (locally smoothed) fitting of the exponential wash-in model to give full-lung wash-in maps for five healthy volunteers.

Dietrich *et. al.* [4] extended the model by adding a variable delay parameter:

$$\begin{aligned} S_{\text{in}}(t) &= (A - B) \exp[-\tau_{\text{in}}(t - t_1 - \Delta t_1)] + B & \Delta t_1 &= \text{delay of wash-in} \\ S_{\text{out}}(t) &= (A - B)(1 - \exp[-\tau_{\text{out}}(t - t_2 - \Delta t_2)]) + B & \Delta t_2 &= \text{delay of wash-out} \end{aligned}$$

In [4], 11 healthy volunteers were scanned with double triggering over 80 frames, making for total durations of 8-12 min. The baseline parameter A was calculated in each voxel as an average of the first 20 frames during air inhalation. The parameters $(\tau_{\text{in}}, \tau_{\text{out}}, \Delta t_0, \Delta t_1, R_{\text{enh}} = A - B)$ were then fitted voxel-wise over frames 21-60 (air- O_2 -air). Sub-models assuming $\tau_{\text{in}} = \tau_{\text{out}}$, $\Delta t_0 = \Delta t_1$, and $\Delta t_0 = \Delta t_1 = 0$ were also tested and ranked according to a corrected Akaike Information Criterion (AICc). The model $\Delta t_0 = \Delta t_1 \neq 0$ is found as optimal for the lung and spleen in combination, with median wash-in/wash-out values $\tau_{\text{in}} = 29.4\text{s}$ and $\tau_{\text{out}} = 25.1\text{s}$ in the lung [4].

Dietrich *et. al.* then used approximations of these values (30s and 25s) for rapid oxygen-responsiveness mapping under a cross-correlation approach. They define the reference series $(r_i)_{i \in [21, \dots, 60]} = S(t_i; R_{\text{enh}}, \tau_{\text{in}} = 30, \tau_{\text{out}} = 25, \Delta t)$ and the raw time series $(q_i)_{i \in [21, \dots, 60]}$ over the relevant time points for each voxel. The voxel-wise optimal delay Δt_{CC} is found as the delay Δt that maximises

$$c_{CC} = \frac{\sum_i^{40} (q_i - \bar{q})(r_i - \bar{r})}{\sqrt{\sum_i^{40} (q_i - \bar{q})^2 \sum_i^{40} (r_i - \bar{r})^2}} \quad (1.1)$$

Voxels with $c_{CC} > 0.5$ were labelled *oxygen-activated*, yielding fractions of 83.6% in the lungs of healthy subjects. Figure 1.4 shows the resulting estimated delays in the lungs and spleen. While a valuable methodology, the median $\tau_{\text{in}}, \tau_{\text{out}}$ values used for the final cross-correlation calculations in [4] were not, in fact, taken from the model performing best in the lung, but the one performing best over an average of lungs and spleen. Furthermore, the same set of wash-in/out rates were used

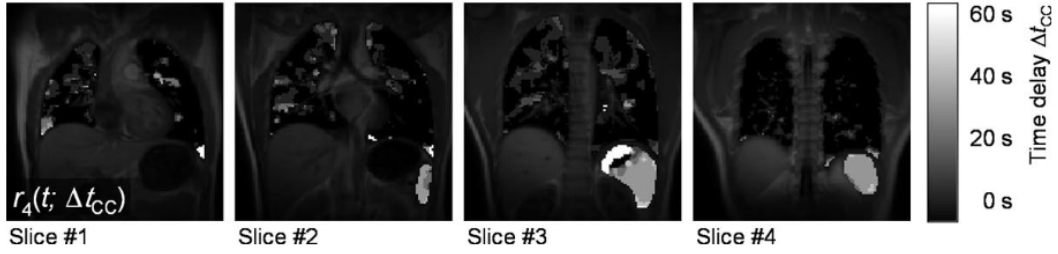


Figure 1.4: From [4]: Voxel-wise shift Δt_{CC} which maximises correlation of exponential function $r_4(t; \Delta t_{CC}) = S(t_i; R_{enh}, \tau_{in} = 30, \tau_{out} = 25, \Delta t_{CC})$ with raw timeseries of voxel, $(q_i)_{i \in [21, \dots, 60]}$

for calculation of the reference series $(r_i)_{i \in [21, \dots, 60]}$ for all voxels. Lastly, the fitted values in [4] may suffer from voxel-wise noise and confounding factors which make estimation of Δt_{CC} unrealistic

In [15], T_2 -weighted images were acquired at time intervals of 1.54 seconds using the optimised dual-echo spoiled-RF gradient echo sequence defined there. Sixteen subjects initially inhaled medical air for 60 time steps (i.e. until $t_0 = 60$), followed by 150 time steps of O_2 inhalation (ending at $t_1 = 210$), and again medical air for another 130 time steps. With A again determined by an average of the first 60 time points in each voxel, they collectively fit the two parameters $\tau = \tau_{in} = \tau_{out}$ and B from the aforementioned model in [18]. While they find good repeatability (scan on same centre) and reproducibility (scan on different centre) for the static signal enhancement – $(B - A)/A$ – across the 16 volunteers, the intra-subject median of constants τ show poor scores. They speculate that the differences are due to the generally low SNR of the O_2 -enhancement in addition to inaccuracies in gas switching times. A similar approach is followed in [19], where no significant differences are found when comparing the median static oxygen-enhancement and wash-in/wash-out parameter τ of healthy volunteers and different sub-groups of ILD patients. Neither [15] nor [19] model separate wash-in/wash-out and neither considers the possibility of a delay in the response to gas switching.

1.5.3 Independent component analysis (ICA)

The signals making up OE-MRI of the lung are composed of multiple sources, including the physiological response to oxygen, respiratory and cardiac motion,

slow drifts, and thermal noise. Independent component analysis (ICA), first applied to such scans in [5], may be used to unmix these sources by assuming that each has a statistically independent marginal distribution in time and that the observed voxel-wise signals are linear combinations of them. The dynamic image series is reshaped into a matrix $\mathbf{X} \in \mathbb{R}^{V \times T}$, where T is the number of time points and V is the number of voxels in a thoracic mask. For *dimensionality* $c \in \mathbb{N}_+$, ICA factorises this matrix as

$$\mathbf{X} \approx \hat{\mathbf{X}} = \mathbf{A} \mathbf{S}, \quad (1.2)$$

where $\hat{\mathbf{X}}$ is the optimal rank- c reconstruction of the time courses in \mathbf{X} , $\mathbf{S} \in \mathbb{R}^{c \times T}$ contains unit variance estimates of the independent temporal components (time series), and $\mathbf{A} \in \mathbb{R}^{V \times c}$ contains the spatial *mixing maps* (one row per voxel). A key point is that by the independence and unit variance of the rows in \mathbf{S} , $\text{Var}(\mathbf{x}_{i,:}) \approx \text{Var}(\hat{\mathbf{x}}_{i,:}) = \sum_j a_{i,j}^2 \text{Var}(\mathbf{s}_j)$. In essence, the weight $a_{i,j}$ is an estimate of the amount of variance in voxel i explained by independent component \mathbf{s}_j .

Using the dual echo sequence developed in [15], Needleman *et. al.* applied ICA to dynamic OE-MRI data acquired with periodic gas switching (air/oxygen cycles) to improve signal separability [5]. In the study, 60 images were acquired during each lobe of a subject inhaling a particular gas for approximately 1.5 minutes. Starting with 60 images acquired during medical air inhalation, O_2 and air were interleaved in this manner for a total of 10.5 minutes (3 oxygen lobes). They scanned 23 subjects, five of which were smokers at the time. Using a particular algorithm for ICA known as *FastICA*, they repeated ICA 51 times ($c \in \{22, \dots, 72\}$) separately on each registered axial slice. For each slice, they compared each of the

$$C = \sum_{i=22}^{72} i = \frac{(72 - 22 + 1)(72 + 22)}{2} = 2397 \quad (1.3)$$

extracted components to a sinusoidal reference representing an idealised time-course of oxygen modulation. The component with highest absolute Spearman correlation against the reference was identified as the "oxygen-enhancement component" (OE-component). The corresponding spatial map $\mathbf{a}_{:,j}$, represents an esti-

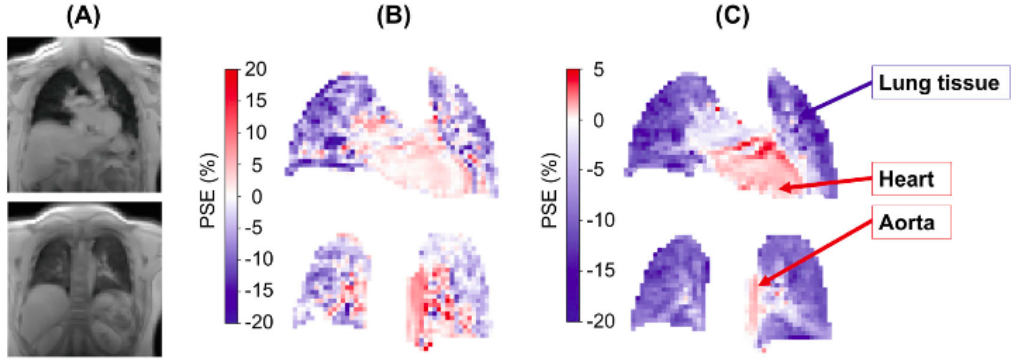


Figure 1.5: From [5]: Two registered MRI images in different slices from the same subject. (B) Percent Signal Enhancement (PSE) maps generated using the (co-registered) raw time series of each voxel. (C) PSE maps using the extracted OE-component for each slice and the associated voxel-wise weights. For each voxel, a mean S_{air} of the raw signal during the initial period of air inhalation was calculated alongside an average S_{oxy} from the last 5 dynamics of each O_2 -delivery lobe. The PSE maps in (B) were then generated as $(S_{oxy} - S_{air})/S_{air}$. A corresponding ratio r_{OE} was calculated for the OE-component s_{OE} shared by all voxels. The PSE maps in (C) were generated by calculating for each voxel i the product $a_{i,OE}r_{OE}$, where $\mathbf{a}_{:,OE}$ is the column-vector of mixing weights for s_{OE} .

mate of the amount of variance in each voxel explained by the selected component. Figure 1.5 shows the percentage signal enhancement for a scan, as calculated using averages of the raw (registered) OE-MRI time series in each voxel and contrasted with a similar calculation using the extracted ICA component and the associated mixing weights $\mathbf{a}_{:,j}$. Across the scans, the extracted component in combination with its weights showed signal decrease in the lung parenchyma (consistent with T_2^* shortening) and signal increase in vascular regions (consistent with T_1 shortening). ICA yielded sharper functional maps (Figure 1.5), reduced motion artefacts, and showed sensitivity to factors such as smoking status, which were not present with simple subtraction maps of the registered images [5].

1.5.4 Identifying Regionally Varying Response Times for OE-MRI

A drawback to the use of temporal ICA mentioned above, however, is that a single time component is identified and associated with the oxygen enhancement for all regions of the lung. While the associated spatial map indicates differing response

intensities, the time course associated with oxygen response (the OE component) of each voxel throughout the lung is the same. This prevents phenomena such as delayed and collateral ventilation from being identified, since the relative intensities of the voxels in the spatial map stay fixed.

In this work, the objective is to implement temporal ICA to capture some of the inevitably variable delays, wash-in and wash-out shapes of the oxygen enhancement response in different regions of the lung. In effect, this work seeks to make the methodologies from [4, 15, 19] more robust to voxel-level noise. In so doing we will also investigate whether the derived parameters are able to distinguish healthy and diseased populations.

The crux is that temporal ICA can be run on subsets of voxels from which separate oxygen-enhancement components may be extracted. Unique oxygen-enhancement components may be generated for each voxel by averaging the components extracted from ICA applied to different subsets.

As mentioned by [15], independent modelling on each voxel is prone to distortion by noise and difficulties in capturing the small intensity changes induced by inhalation of pure oxygen [4]. By contrast ICA is able to capture region-wide modulations to the signal.

Chapter 2

Independent Component Analysis

2.1 Outline of FastICA

This section will outline the workings of temporal independent component analysis (ICA) and more importantly the FastICA algorithm that is used here to identify the oxygen-enhancement response from dynamic OE-MRI scans. Understanding the algorithm and the underlying mathematics are necessary to justify the way it will be used in this report. It should be noted here that FastICA is by no means the only algorithm for carrying out temporal ICA: other algorithms include Infomax ICA, ICA by joint approximate diagonalisation of eigenmatrices (JADE), and ICA by maximum likelihood maximisation [20]. However, each method relies on the same fundamental principles. The benefit of FastICA is that it has a well-documented and stable implementation in `scikit-learn` [21].

2.1.1 Overview

ICA falls into the category of blind source separation techniques in signal processing. Such methods attempt to extract source signals when only a mixture of those signals are observable. In the case of ICA, the values from different source signals at each sampling point t are assumed to be samples from statistically independent distributions. In the case of linear ICA, the source signals are also taken to combine linearly to produce the observed mixtures. When referring to ICA in this text, we shall take it to mean linear ICA unless otherwise noted. Crucially, ICA requires the number of independent components sought to be specified, and in some implemen-

tations this number may have an upper bound.

2.1.2 Mathematical Formulation

Consider a matrix $\mathbf{X} \in \mathbb{R}^{V \times T}$ containing V discretely sampled signals over T sampling points. For MRI purposes one may imagine the time-courses of V voxels. ICA seeks matrices \mathbf{S} and \mathbf{A} such that

$$\mathbf{X} \approx \mathbf{AS}, \quad (2.1)$$

where the rows of $\mathbf{S} \in \mathbb{R}^{c \times T}$ are the statistically independent components (ICs), c is the desired number of such components, and $\mathbf{A} \in \mathbb{R}^{V \times c}$ holds the "mixing weights" for each sampled vector. In the MRI analogy, the extracted ICs in \mathbf{S} constitute independent time series. Similarly, each row i of \mathbf{A} holds the weights needed to approximately reconstruct the time course of voxel i as a weighted sum of the ICs. When ICA is used in this way on temporal data to extract independent time series, it is often called *temporal ICA*.

By contrast, *spatial ICA* seeks $\hat{\mathbf{S}}$ and $\hat{\mathbf{A}}$ such that

$$\mathbf{X}^\top \approx \hat{\mathbf{A}}\hat{\mathbf{S}}. \quad (2.2)$$

In this latter scenario, the ICs on the rows of $\hat{\mathbf{S}} \in \mathbb{R}^{c \times V}$ would represent independent "spatial maps" (voxel maps in the case of dynamic MRI).

It is important to note, however, that ICA is applicable in many situations where there may be no temporal or spatial dimension; the crux is that independent components along one dimension combine linearly with weights along another to approximately reconstruct the observed signals. In this text, we will be referring to temporal ICA when mentioning ICA.

2.1.3 Independence and Independent Components

In ICA, each independent component, or equivalently, row i of the matrix \mathbf{S} is considered a set of realisations, $\{s_1^{(i)}, \dots, s_T^{(i)}\}$, of a random variable $S_i \sim p_{S_i}(s)$. The algorithm seeks $\mathbf{X} \approx \mathbf{AS}$ under the constraint that at each sampling point t , the un-

derlying random variables $\{S_1, \dots, S_c\}$, are mutually independent;

$$p(s_t^{(1)}, \dots, s_t^{(c)}) = \prod_{i=1}^c p_{S_i}(s_t^{(i)}). \quad (2.3)$$

Note that we can only implicitly monitor approximate mutual independence, as it must be inferred from the realisations $s_t^{(i)}$, which are adjusted during the ICA algorithm. It must be emphasised that independence is enforced *only* across components at the same sampling point. Therefore, ICA does *not* enforce

$$p_{S_i}(s_i(t)|s_i(t+\tau)) = p_{S_i}(s_i(t)), \quad \tau \neq 0. \quad (2.4)$$

In other words, a single component may still exhibit temporal autocorrelation or dependence on itself. Furthermore, ICA does not enforce

$$p_{S_i}(s_i(t)|s_k(t+\tau)) = p_{S_i}(s_i(t)), \quad \tau \neq 0, i \neq k, \quad (2.5)$$

meaning two different components can remain statistically related at different sampling points (lags). ICA therefore guarantees independence only "vertically" (across components at one instant); any "horizontal" dependencies over time (within or between components) are outside its scope and would require an extension of the technique. However, as noted by Hyvarinen [20], the technique has been successfully used to approximately reconstruct generating signals from unknown mixtures in a number of disciplines, and the assumption of instantaneous independence is usually enough.

2.1.4 Ambiguities

From the desired approximate inequality $\mathbf{X} \approx \mathbf{AS}$ and the fact that independence is invariant to scaling, it is easily seen that a solution \mathbf{A}, \mathbf{S} remains perfectly valid for arbitrary column scalings of \mathbf{A} as long as these are matched by the inverse scalings on the corresponding rows of \mathbf{S} . To dispense with this ambiguity, any ICA implementation usually requires that the variances of the independent components (rows of \mathbf{S}) are unity.

Furthermore, it should be noted that the order and sign of the extracted components is arbitrary. This can be seen since:

$$(\mathbf{AP})(\mathbf{P}^{-1}\mathbf{S}) = \mathbf{AS} \quad (2.6)$$

for any signed permutation matrix \mathbf{P} .

2.1.5 Algorithm

In this section, we will describe and loosely justify the FastICA algorithm as implemented in `scikit-learn`. The algorithm was developed by Aapo Hyvärinen at Helsinki University of Technology, and readers interested in a more rigorous approach should consult his work [20, 22, 23].

Consider again a matrix $\mathbf{X} \in \mathbb{R}^{V \times T}$ representing some process in time across V *probes* and let $c \in \{1, \dots, V\}$. The algorithm begins by centering the time series in each probe about zero;

$$\bar{\mathbf{X}} \leftarrow \mathbf{X}\mathbf{H}_T, \quad \text{with } \mathbf{H}_T = \mathbf{I}_T - \frac{1}{T}\mathbf{1}\mathbf{1}_T^\top \quad \text{and } \mathbf{1}_T = (1 \ 1 \ \dots \ 1)^\top \in \mathbb{R}^T. \quad (2.7)$$

This centering simplifies later steps, and we shall see that it has no bearing on the quality of the final result. Second, the centred matrix is linearly transformed so that its retained timeseries covariances become the identity. By the spectral theorem we may write

$$\frac{1}{T}\bar{\mathbf{X}}\bar{\mathbf{X}}^\top = \mathbf{E}\mathbf{D}\mathbf{E}^\top, \quad (2.8)$$

for $\mathbf{D} = \text{diag}(\lambda_1, \dots, \lambda_V)$ containing the eigenvalues of $T^{-1}\bar{\mathbf{X}}\bar{\mathbf{X}}^\top$ in descending order and $\mathbf{E} = [\mathbf{v}_1, \dots, \mathbf{v}_V]$ the corresponding eigen-vectors. We may then write

$$\mathbf{D} = \begin{pmatrix} \mathbf{D}_{\parallel} & \mathbf{0} \\ \mathbf{0} & \mathbf{D}_{\perp} \end{pmatrix} \quad \text{and} \quad \mathbf{E} = \begin{pmatrix} \mathbf{E}_{\parallel} & \mathbf{E}_{\perp} \end{pmatrix} \quad (2.9)$$

where $\mathbf{D}_{\parallel} = \text{diag}(\lambda_1, \dots, \lambda_c)$ and $\mathbf{E}_{\parallel} = [\mathbf{v}_1, \dots, \mathbf{v}_c]$. The *whitened* data are then taken as

$$\mathbf{Z} \leftarrow \mathbf{D}_{\parallel}^{-1/2}\mathbf{E}_{\parallel}^\top\bar{\mathbf{X}}. \quad (2.10)$$

It may be found that the resulting matrix $\mathbf{Z} \in \mathbb{R}^{c \times T}$ has rows with mean zero (since $\bar{\mathbf{X}}$ was only left-multiplied), satisfies $\mathbf{Z}\mathbf{Z}^\top = T\mathbf{I}_c$, and therefore has uncorrelated rows with variance one. In fact, the rows of \mathbf{Z} are the normalised projections of $\bar{\mathbf{X}}$ onto the first c principal components. (In the MRI analogy, they are the time courses associated with the first c spatial principal components.) The number c of components that will be extracted therefore corresponds also to the number of dimensions retained in the data.

After whitening, any further linear mixture $\mathbf{W}^\top \mathbf{Z}$, $\mathbf{W} \in \mathbb{R}^{c \times c}$ that preserves uncorrelatedness and unit variance of the rows must be an orthogonal rotation (i.e. $\mathbf{W}^\top \mathbf{W} = \mathbf{I}_c$). The main difficulty in ICA is reduced to finding such a rotation that makes the resulting rows of $\mathbf{S} = \mathbf{W}^\top \mathbf{Z}$ maximally independent [20]. That step will be covered separately in the next section.

Having found \mathbf{W} , one may define $\mathbf{A} = \mathbf{E}_{\parallel} \mathbf{D}_{\parallel}^{1/2} \mathbf{W}$, such that we see

$$\mathbf{AS} = \mathbf{E}_{\parallel} \mathbf{D}_{\parallel}^{1/2} \mathbf{Z} = \mathbf{E}_{\parallel} \mathbf{E}_{\parallel}^\top \bar{\mathbf{X}} \approx \bar{\mathbf{X}}. \quad (2.11)$$

At this point, we note that $\mathbf{R} = \mathbf{E}_{\parallel} \mathbf{E}_{\parallel}^\top \in \mathbb{R}^{V \times V}$ is the matrix projecting $\bar{\mathbf{X}}$ onto the space spanned by the eigenvectors in \mathbf{E}_{\parallel} . The product $\mathbf{E}_{\parallel} \mathbf{E}_{\parallel}^\top \bar{\mathbf{X}}$ is therefore the best rank- c representation of $\bar{\mathbf{X}}$.

To make the final connection back to the initial matrix \mathbf{X} , note that given some solution $\mathbf{S} = \mathbf{W}^\top \mathbf{Z}$, we also have

$$\mathbf{W}^\top \mathbf{D}_{\parallel}^{-1/2} \mathbf{E}_{\parallel}^\top \mathbf{X} \mathbf{H}_T = \mathbf{S} \quad (2.12)$$

$$\Rightarrow \mathbf{W}^\top \mathbf{D}_{\parallel}^{-1/2} \mathbf{E}_{\parallel}^\top \mathbf{X} = \mathbf{S} + \frac{1}{T} \mathbf{W}^\top \mathbf{D}_{\parallel}^{-1/2} \mathbf{E}_{\parallel}^\top \mathbf{X} \mathbf{1}_T \mathbf{1}_T^\top \quad (2.13)$$

$$\Rightarrow \mathbf{E}_{\parallel} \mathbf{E}_{\parallel}^\top \mathbf{X} = \mathbf{A} \left(\mathbf{S} + \frac{1}{T} \mathbf{W}^\top \mathbf{D}_{\parallel}^{-1/2} \mathbf{E}_{\parallel}^\top \mathbf{X} \mathbf{1}_T \mathbf{1}_T^\top \right) \quad (2.14)$$

$$\Rightarrow \mathbf{X} \approx \mathbf{AS} \quad (2.15)$$

Now, the rows of $\dot{\mathbf{S}} = (\mathbf{S} + \mathbf{W}^\top \mathbf{D}_{\parallel}^{-1/2} \mathbf{E}_{\parallel}^\top \mathbf{X} \mathbf{1}_T \mathbf{1}_T^\top)$ remain equally independent as those in \mathbf{S} , since only a constant is added.

2.2 Finding the Independent Components

To understand the process with which independent components are estimated in any ICA algorithm (not just FastICA), it is necessary to understand the need for non-Gaussianity and the associated concept of negentropy.

2.2.1 Non-Gaussianity

It can be shown that at most one independent component can have a Gaussian distribution $p_{S_i}(s)$ if the model is to remain identifiable. Loosely speaking, this is a consequence of the fact that a sum of independent Gaussians is again Gaussian, but more importantly rotationally symmetric.

In the ICA model we posit an unobserved random vector $S = (S_1, \dots, S_c)^\top$ whose components are mutually independent, zero-mean and unit-variance. After centering and whitening the data matrix $\mathbf{X} \in \mathbb{R}^{V \times T}$, we obtain

$$\mathbf{Z} = [\mathbf{z}_{:,1}, \dots, \mathbf{z}_{:,T}] \in \mathbb{R}^{c \times T},$$

where each column $\mathbf{z}_{:,t}$ is assumed to be one realisation of the random vector $Z = (Z_1, \dots, Z_c)^\top$, in which the variables are uncorrelated, have mean zero, and variance one. The assumption is that there exists a unique¹ orthogonal matrix $\mathbf{W} \in \mathbb{R}^{c \times c}$ such that the implicit variables

$$S = \mathbf{W}^\top Z \quad (\text{equivalently } Z = \mathbf{W}S) \tag{2.16}$$

are mutually independent. Because right-multiplying \mathbf{W} by any signed permutation matrix \mathbf{P} only re-orders and/or flips the signs of the components, any solution (\mathbf{W}, S) that satisfies (2.16) also yields $(\mathbf{WP}^\top, \mathbf{PS})$ an equally valid solution.

Now, assume that we allow two Gaussian sources $S_1, S_2 \stackrel{\text{i.i.d.}}{\sim} \mathcal{N}(0, 1)$ and consider some solution $\mathbf{W}^{(1)}$. Let

$$\mathbf{B} = \begin{pmatrix} \mathbf{M}_\theta & \mathbf{0} \\ \mathbf{0} & \mathbf{I}_{c-2} \end{pmatrix} \quad \text{and} \quad \mathbf{M}_\theta = \begin{pmatrix} \cos \theta & -\sin \theta \\ \sin \theta & \cos \theta \end{pmatrix}, \tag{2.17}$$

¹up to signed permutation

with $\theta \notin \{k\pi/2 | k \in \mathbb{N}\}$. Any orthogonal mixture of independent $\mathcal{N}(0, 1)$ variables is again i.i.d $\mathcal{N}(0, 1)$ (this is a fundamental property of Gaussian variables [22]). Hence, we see that $\mathbf{W}^{(1)}S$ has precisely the same distribution as $\mathbf{W}^{(1)}\mathbf{B}S$, since $\mathbf{W}^{(1)}\mathbf{B}$ is again orthogonal. In other words, $\mathbf{W}^{(1)} \neq \mathbf{W}^{(2)} = \mathbf{W}^{(1)}\mathbf{B}$ are equally valid solutions despite not being signed permutations of the same matrix. It follows that allowing two Gaussian sources leaves the ICA model continuously rotationally ambiguous (since θ can vary continuously). The argument straightforwardly extends to several Gaussian sources. Hence, non-Gaussianity in all but at most one source is necessary to eliminate continuous ambiguity.

2.2.2 Measures of Gaussianity

To make sure we have no more than one Gaussian variable, we need to be able to continuously quantify the degree of "Gaussianity" of a variable. There are a number of metrics defined on random variables designed to measure how "close" the distribution of that variable is to being Gaussian. One of these measures is entropy, which is defined on a continuous variable Y with support \mathcal{Y} as

$$H(Y) = - \int_{\mathcal{Y}} p_Y(y) \log(p(y)) dy. \quad (2.18)$$

It may be shown that the largest entropy of any continuous random variable with a given variance is the Gaussian [20]. Negentropy of a random variable Y is defined as,

$$J(Y) = H(Y_{Gauss}) - H(Y), \quad (2.19)$$

where Y_{Gauss} is a Gaussian of equal variance to Y . Hence, the smallest possible negentropy of zero at a particular variance is held by the Gaussian. Negentropy is therefore a continuous measure of the (non-)Gaussianity of a random variable. Many estimates of negentropy exist, but Hyvarinen uses the approximation

$$J(Y) \propto [\mathbb{E}(G(Y)) - \mathbb{E}(G(Y_{Gauss}))]^2, \quad (2.20)$$

where G can take on the form of certain non-quadratic functions. Some useful choices (used in `scikit-learn`'s FastICA) are $G(Y) = a_1^{-1} \log(\cosh(a_1 Y))$, $1 \leq a_1 \leq 2$ and $G(Y) = -\exp(Y^2/2)$.

In most cases, we do not have access to the density of the variable Y , and negentropy must be estimated using realisations $\{y_1, \dots, y_T\}$ of the variable as

$$J(Y) \approx [\frac{1}{T} \sum_{i=1}^T G(y_i) - \mathbb{E}(G(Y_{Gauss}))]^2 \quad (2.21)$$

2.2.3 Uniqueness of the Solution

We will show now that with at most one non-Gaussian source, the ICA model indeed has at most one correct mixing matrix \mathbf{W} , up to signed permutation.

Assume that S is the vector of true independent source variables and \mathbf{W} is the orthogonal mixing matrix such that $S = \mathbf{W}^\top Z$, with Z the underlying random vector of the whitened data.

Now, consider some other orthonormal matrix $\hat{\mathbf{W}}$ which is not a mere signed column-permutation of the rows of \mathbf{W} . Let $\hat{S} = \hat{\mathbf{W}}^\top Z$. It follows that

$$\hat{S} = \hat{\mathbf{W}}^\top Z = \hat{\mathbf{W}}^\top \mathbf{W} S \quad (2.22)$$

$$\Rightarrow \hat{S} = \mathbf{B} S, \quad (\mathbf{B} = \hat{\mathbf{W}}^\top \mathbf{W} \text{ is orthogonal}). \quad (2.23)$$

By definition of the matrix $\hat{\mathbf{W}}$, $\mathbf{B} = \hat{\mathbf{W}}^\top \mathbf{W}$ must have at least two rows with non-zeros in two or more of the same columns. Hence at least two rows of $\hat{S} = \mathbf{B} S$ are non-trivial linear mixtures involving some components S_i and S_j from S . Since at most one of S_i and S_j can be Gaussian, the Darmois–Skitovich theorem² [24] then implies that such a mixture cannot render the two resulting mixtures independent. Thus the resulting rows of \hat{S} cannot all be mutually independent. Independence therefore singles out, up to sign and permutation, the unique rotation \mathbf{W}^\top that places

²The theorem states that if $Y_1, \dots, Y_n, n \geq 2$ are independent random variables and $\alpha_1, \dots, \alpha_n, \beta_1, \dots, \beta_n$ constants satisfying $\alpha_i \beta_i \neq 0$ for at least two i , then the sum $L_1 = \sum_i \alpha_i Y_i, L_2 = \sum_i \beta_i Y_i$ are independent if, and only if Y_1, \dots, Y_n are all Gaussian. A remarkable theorem indeed!

each non-Gaussian source in a separate row, with one Gaussian row allowed but indeterminate.

2.2.4 Why Maximise Non-Gaussianity

By the entropy power inequality and Jensen's inequality, one can show that, for independent unit-variance variables Y_1, \dots, Y_m , at least one of which is non-Gaussian, any non-trivial linear sum $Y = \sum_i a_i Y_i$, $\sum_i a_i^2 = 1$, $a_i \neq 0 \forall i \in \{1, \dots, m\}$ with $\sum_i a_i^2 = 1$ satisfies

$$J(Y) < \sum_i a_i^2 J(Y_i), \quad (2.24)$$

where again $J(\cdot)$ denotes the negentropy [25]. In ICA, it follows that any variable Z_i which is a non-trivial orthogonal projection (sum) of the true source variables S_1, \dots, S_c has a smaller negentropy than the maximum among its parts.

We shall now see that maximising the total negentropy (non-Gaussianity) over all variables is equivalent to finding a solution $\tilde{\mathbf{W}}$ which is a signed column permutation of the solution \mathbf{W} from before. With \hat{S} , $\hat{\mathbf{W}}$ and \mathbf{B} as before, note that

$$\sum_{i=1}^c J(\hat{S}_i) = \sum_{i=1}^c J(\mathbf{b}_{i,:} S) \quad (2.25)$$

$$< \sum_{i=1}^c \sum_{j=1}^c b_{i,j}^2 J(S_j) \quad (\text{Entropy Power Inequality}) \quad (2.26)$$

$$= \sum_{j=1}^c J(S_j) \sum_{i=1}^c b_{i,j}^2 \quad (2.27)$$

$$= \sum_{j=1}^c J(S_j). \quad (2.28)$$

Hence, negentropy cannot be maximised for any $\hat{\mathbf{W}}$ which is not a signed column-permutation of \mathbf{W} .

2.2.5 Iterative Maximisation of Negentropy

See that $S_i = (\mathbf{w}_{:,i})^\top Z$. Hence, the random variable S_i depends only on a single column in \mathbf{W} . It is these columns that we adjust iteratively in FastICA, in order to

make the underlying variables S_i as independent as possible. See that

$$J(S_i) \propto \hat{J}(S_i) = [\mathbb{E}(G[Y_i]) - \mathbb{E}(G[Y_{Gauss}])]^2 = [\mathbb{E}(G[(\mathbf{w}_{:,i})^\top \mathbf{Z}]) - \mathbb{E}(G[Y_{Gauss}])]^2, \quad (2.29)$$

Due to the dependence of each S_i on only a single column in \mathbf{W} , the overall negentropy may be maximised by individually maximising the estimated negentropies $\hat{J}(S_i)$, while maintaining orthogonality of \mathbf{W} . Each maximum of the estimate $\hat{J}(S_i)$ corresponds to an extremum of $\mathbb{E}(G[(\mathbf{w}_{:,i})^\top \mathbf{Z}])$. Since we do not have access to the underlying variables S_i , however, we must work with the estimator

$$\frac{1}{T} \sum_{j=1}^T G((\mathbf{w}_{:,i})^\top \mathbf{z}_{:,j}) = \frac{G[(\mathbf{w}_{:,i})^\top \mathbf{Z}] \mathbf{1}_c}{T}, \quad (2.30)$$

where the function G is applied element-wise on the row-vector $(\mathbf{w}_{:,i})^\top \mathbf{Z}$. Focusing now on a given source S_i , we write $\mathbf{w}_{:,i} = \mathbf{w}$. The Lagrangian to the problem of finding extrema of (2.30) under the constraint that $\|\mathbf{w}\|_2 = 1$ is

$$\mathcal{L} = \frac{G[\mathbf{w}^\top \mathbf{Z}] \mathbf{1}_c}{T} - \frac{\lambda}{2} (\mathbf{w}^\top \mathbf{w} - 1) \quad (2.31)$$

Taking the gradient with respect to the vector \mathbf{w} yields

$$\nabla_{\mathbf{w}} \mathcal{L} = \frac{1}{T} \mathbf{Z} g[\mathbf{Z}^\top \mathbf{w}] - \lambda \mathbf{w} \quad (2.32)$$

where again the derivative g is applied element-wise on the vector $\mathbf{Z}^\top \mathbf{w}$. The corresponding Jacobian is then

$$\mathbf{J}_{\mathbf{w}}(\mathcal{L}) = \frac{1}{T} \mathbf{Z} \operatorname{diag}(g'[\mathbf{Z}^\top \mathbf{w}]) \mathbf{Z}^\top - \lambda \mathbf{I}_c \quad (2.33)$$

Let

$$H(\mathbf{w}) = \frac{1}{T} \mathbf{Z} \operatorname{diag}(g'[\mathbf{Z}^\top \mathbf{w}]) \mathbf{Z}^\top. \quad (2.34)$$

Note now that for $k, l \in \{1, \dots, c\}$ and sufficiently large T ,

$$[H(\mathbf{w})]_{k,l} = \frac{1}{T} \sum_{j=1}^T g'(\mathbf{w}^\top \mathbf{z}_{:,j}) z_{k,j} z_{l,j} \quad (2.35)$$

$$\approx \mathbb{E}[g'(\mathbf{w}^\top Z) Z_k Z_l] \quad (2.36)$$

when, as mentioned, we consider the columns in \mathbf{Z} realisations of the random vector Z . Because the data are whitened ($\mathbb{E}[Z_k Z_\ell] = \delta_{k\ell}$), one can make the assumption that the variable ($y = \mathbf{w}^\top Z$) is only weakly dependent on the component $Z_\perp = Z - \mathbf{w}^\top Z \mathbf{w}$ orthogonal to \mathbf{w} . Hyvärinen [20] therefore approximates

$$\mathbb{E}\left[g'(\mathbf{w}^\top Z) Z_k Z_\ell\right] \approx \mathbb{E}\left[g'(\mathbf{w}^\top Z)\right] \mathbb{E}[Z_k Z_\ell].$$

By the whitened properties of Z , it follows that

$$\mathbb{E}[g'(\mathbf{w}^\top Z) Z_k Z_l] \approx \begin{cases} 0, & k \neq l \\ \mathbb{E}[g'(\mathbf{w}^\top Z)], & k = l \end{cases}. \quad (2.37)$$

Going back to our terms $H(\mathbf{w})$ and $\mathbf{J}_\mathbf{w}(\mathcal{L})$, we therefore write

$$H(\mathbf{w}) \approx \frac{g'(\mathbf{w}^\top \mathbf{Z}) \mathbf{1}_c}{T} \mathbf{I}_c \quad \Rightarrow \quad \mathbf{J}_\mathbf{w}(\mathcal{L}) \approx \left(\frac{1}{T} (g'[\mathbf{w}^\top \mathbf{Z}] \mathbf{1}_c) - \lambda \right) \mathbf{I}_c \quad (2.38)$$

The crucial point is that this approximation makes $\mathbf{J}_\mathbf{w}(\mathcal{L})$ a diagonal matrix which can easily be inverted. Using this approximation, we can then solve for the zeros of (2.32) in an iterative manner using Newton's method. We initialise some unit norm vector $\mathbf{w}^{(0)} \in \mathbb{R}^c$. By the Newton method, we have

$$\mathbf{w}^{(k+1)} = \mathbf{w}^{(k)} - (\mathbf{J}_\mathbf{w}(\mathcal{L}))^{-1} \nabla_{\mathbf{w}} \mathcal{L} \quad (2.39)$$

Using the approximation for $\mathbf{J}_\mathbf{w}(\mathcal{L})$, we get

$$\mathbf{w}^{(k+1)} = \mathbf{w}^{(k)} - \left(\frac{1}{T} \mathbf{Z} g[\mathbf{Z}^\top \mathbf{w}] - \lambda \mathbf{w} \right) / \left(\frac{1}{T} \mathbf{1}_c^\top g'[\mathbf{Z}^\top \mathbf{w}^{(k)}] - \lambda \right) \quad (2.40)$$

See now that multiplying both sides by $\lambda - \frac{1}{T} \mathbf{1}_c^\top g'[\mathbf{Z}^\top \mathbf{w}^{(k)}]$ yields

$$\left(\lambda - \frac{1}{T} \mathbf{1}_c^\top g'[\mathbf{Z}^\top \mathbf{w}^{(k)}] \right) \mathbf{w}^{(k+1)} = \frac{1}{T} \mathbf{Z}g[\mathbf{Z}^\top \mathbf{w}^{(k)}] - \frac{1}{T} \mathbf{1}_c^\top g'[\mathbf{Z}^\top \mathbf{w}^{(k)}] \mathbf{w}^{(k)}. \quad (2.41)$$

Finally, note that the final update $\mathbf{w}^{(k+1)}$ can simply be normalised before the next iteration. It follows that the scalar factor $\lambda - \frac{1}{T} \mathbf{1}_c^\top g'[\mathbf{Z}^\top \mathbf{w}^{(k)}]$ on the left-hand side is completely irrelevant as long as we normalise after each iteration. Hence, we get the update scheme

$$1. \quad \mathbf{w}^{(k+1)} = \frac{1}{T} \mathbf{Z}g[\mathbf{Z}^\top \mathbf{w}^{(k)}] - \frac{1}{T} \mathbf{1}_c^\top g'[\mathbf{Z}^\top \mathbf{w}^{(k)}] \mathbf{w}^{(k)} \quad (2.42)$$

$$2. \quad \mathbf{w}^{(k+1)} = \mathbf{w}^{(k+1)} / \|\mathbf{w}^{(k+1)}\|_2 \quad (2.43)$$

If we are interested only in the realisations $\mathbf{s}_{i,:}$ of a single variable S_i , this simple process can be repeated until $|(\mathbf{w}^{(k+1)})^\top \mathbf{w}^{(k)} - 1| < \varepsilon$ for some tolerance ε . When we desire multiple components, however, we must ensure that the columns $\mathbf{w}_{:,i}$ are perpendicular. Having extracted p columns, we can simply use Gram-Schmidt orthogonalisation in the second step followed by normalisation in the third. Drawing together all we have learned so far, the "deflationary" FastICA Algorithm 1 appears. It is called deflationary because we gradually exhaust the number of possible directions in the c -dimensional space for each new mixing column \mathbf{w} . In some cases, however, we are interested in finding the independent components all at once, such that they receive equal priority during the Newton algorithm. In that case, the update in (2.42) can be applied to all columns of \mathbf{W} at once as

$$\mathbf{W}^{(+)} = \frac{1}{T} \mathbf{Z}g(\mathbf{Z}^\top \mathbf{W}) - \frac{1}{T} \mathbf{W} \text{diag}[\mathbf{1}_T^\top g'(\mathbf{Z}^\top \mathbf{W})]. \quad (2.44)$$

One may then use the conventional matrix orthogonalisation procedure

$$\mathbf{W} = [\mathbf{W}^{(+)} (\mathbf{W}^{(+)})^\top]^{-1/2} \mathbf{W}^{(+)}. \quad (2.45)$$

The "symmetric" fastICA algorithm then appears as in Algorithm 2.

Algorithm 1 Deflationary FastICA [20]

Require: Data matrix $\mathbf{X} \in \mathbb{R}^{V \times T}$ (observed sources in rows, sampling-points in columns); number of components $c \leq V$; non-linear function $g(u)$ with derivative $g'(u)$; tolerance $\varepsilon > 0$.

- 1: **Center** the data: $\bar{\mathbf{X}} \leftarrow \mathbf{X}(\mathbf{I}_T - \frac{1}{T}\mathbf{1}_T\mathbf{1}_T^\top)$
- 2: **Whiten:** $\frac{1}{T}\bar{\mathbf{X}}\bar{\mathbf{X}}^\top = \mathbf{E}\mathbf{D}\mathbf{E}^\top$, $\mathbf{Z} \leftarrow \mathbf{D}_{1:c,1:c}^{-1/2}\mathbf{E}_{:,1:c}^\top\bar{\mathbf{X}}$
- 3: $\mathbf{W} \leftarrow \mathbf{0}_{c \times c}$ ▷ to store the c unmixing vectors
- 4: **for** $p = 1$ **to** c **do** ▷ deflation loop
- 5: Init. $\mathbf{w}^{(0)} \sim \mathcal{N}[-1, 1]^c$; normalise: $\mathbf{w}^{(0)} \leftarrow \mathbf{w}^{(0)}/\|\mathbf{w}^{(0)}\|$, $k \leftarrow 0$
- 6: **repeat** ▷ fixed-point iteration
- 7: $\mathbf{w}^+ \leftarrow \frac{1}{T}\mathbf{Z}g(\mathbf{Z}^\top\mathbf{w}^{(k)}) - \frac{1}{T}\mathbf{1}_c^\top g'(\mathbf{Z}^\top\mathbf{w}^{(k)})\mathbf{w}^{(k)}$
- 8: $\mathbf{w}^+ \leftarrow \mathbf{w}^+ - \sum_{q=1}^{p-1} (\mathbf{w}_{q,:}^\top\mathbf{w}^+) \mathbf{w}_{q,:}$ ▷ Gram–Schmidt
- 9: $\mathbf{w}^{(k+1)} \leftarrow \mathbf{w}^+/\|\mathbf{w}^+\|$ ▷ Normalise
- 10: $k \leftarrow k + 1$
- 11: **until** $|(\mathbf{w}^{(k)})^\top\mathbf{w}^{(k-1)}| > 1 - \varepsilon$
- 12: $\mathbf{W}_{:,p} \leftarrow (\mathbf{w}^{(k)})^\top$ ▷ store the p -th component
- 13: **end for**
- 14: $\mathbf{A} \leftarrow \mathbf{E}_{:,1:c}\mathbf{D}_{1:c,1:c}^{1/2}\mathbf{W}$ ▷ Project mixing matrix into variable space
- 15: **return** matrix $\mathbf{A} \in \mathbb{R}^{V \times c}$, sources $\mathbf{S} = \mathbf{W}^\top\mathbf{Z}$

Algorithm 2 Symmetric FastICA [20]

Require: Data matrix $\mathbf{X} \in \mathbb{R}^{V \times T}$ (observed sources in rows, sampling-points in columns); number of components $c \leq V$; non-linear function $g(u)$ with derivative $g'(u)$; tolerance $\varepsilon > 0$.

- 1: **Center** the data: $\bar{\mathbf{X}} \leftarrow \mathbf{X}(\mathbf{I}_T - \frac{1}{T}\mathbf{1}_T\mathbf{1}_T^\top)$
- 2: **Whiten:** $\frac{1}{T}\bar{\mathbf{X}}\bar{\mathbf{X}}^\top = \mathbf{E}\mathbf{D}\mathbf{E}^\top$, $\mathbf{Z} \leftarrow \mathbf{D}_{1:c,1:c}^{-1/2}\mathbf{E}_{:,1:c}^\top\bar{\mathbf{X}}$
- 3: $k \leftarrow 0$
- 4: Initialise $\mathbf{W}^{(0)} \sim \mathcal{N}(0, 1)^{c \times c}$
- 5: $\mathbf{W}^{(0)} \leftarrow (\mathbf{W}^{(0)}\mathbf{W}^{(0)\top})^{-\frac{1}{2}}\mathbf{W}^{(0)}$ ▷ Symmetrically Orthogonalise
- 6: **repeat**
- 7: $\mathbf{W}^{(+)} \leftarrow \frac{1}{T}\mathbf{Z}g(\mathbf{Z}^\top\mathbf{W}^{(k)})^\top - \frac{1}{T}\mathbf{W}^{(k)} \text{ diag}[\mathbf{1}_T^\top g'(\mathbf{Z}^\top\mathbf{W}^{(k)})]$
- 8: $\mathbf{W}^{(k+1)} \leftarrow (\mathbf{W}^{(+)}\mathbf{W}^{(+)\top})^{-\frac{1}{2}}\mathbf{W}^{(+)}$
- 9: $k \leftarrow k + 1$
- 10: **until** $\min_j |(\mathbf{w}_{:,j}^{(k)})^\top\mathbf{w}_{:,j}^{(k-1)}| > 1 - \varepsilon$
- 11: $\mathbf{A} \leftarrow \mathbf{E}_{:,1:c}\mathbf{D}_{1:c,1:c}^{1/2}\mathbf{W}$ ▷ Project unmixing mixing matrix into variable space
- 12: **return** matrix $\mathbf{A} \in \mathbb{R}^{V \times c}$, sources $\mathbf{S} = \mathbf{W}^\top\mathbf{Z}$

Chapter 3

Spatially Averaged Temporal ICA for OE-MRI

We describe here a proposed method for identifying spatially varying, yet robust, oxygen-enhancement time courses for OE-MRI of the human lung. The method rests on iteratively applying temporal ICA to the time series of voxels within a window sliding spatially across the region of interest. The reasoning behind this method is that the shape and delay of oxygen enhancement could vary significantly within the lung. As demonstrated in [5], the varying noise and confounding factors present in each voxel limit the reliability of estimates about oxygen response based on analysis of each time series in isolation. However, the ability of the ICA method used in [5] to identify an OE component gives promise for more robust estimation when time courses of several voxels are considered together. To achieve reliable, yet regionally varying oxygen responses, we therefore do ICA on smaller sets (windows) of neighbouring voxels throughout the lung.

In this chapter, we will discuss the mathematical nature of the method and outline the ambiguities within it. We will then motivate and show the results of an experiment designed to explore the consequences of different parameter combinations on the OE-MRI scan of a healthy individual. Lastly, we will describe the full pipeline for the proposed method with practical restrictions on the parameter space informed by the earlier experiment.

3.1 Windowed ICA in the Literature

To the best of the author’s knowledge, temporal ICA applied repeatedly on a sliding spatial window has not been applied in the literature. However, a number of studies from the MEG/EEG and fMRI literature have used sliding *temporal* windows with spatial ICA applied to the set of images within each temporal window. Partially overlapping temporal windows allow the resulting spatial maps and their accompanying time courses to wax, wane or re-configure as the window moves. The technique was first illustrated for EEG scans, where Makeig and co-authors recomputed spatial ICA in a 3s sliding *temporal* window to follow millisecond-scale changes in EEG sources [26]. It was later transferred to fMRI: Esposito et al. repeated spatial ICA in sliding temporal windows containing 10 images at a time, collected over 20 seconds, and showed that functionally connected brain regions could be identified in real-time as a subject was carrying out tasks over a specified interval [27]. A number of studies have later used the method to assess functional connectivity [28, 29].

3.2 Theoretical Overview

3.2.1 The Sliding Window

Consider a two-dimensional dynamic OE-MRI scan collected over $T \in \mathbb{N}$ time points and over V voxels. The dynamic data may be represented by the matrix $\mathbf{X} \in \mathbb{R}^{V \times T}$ where \mathbf{X} is assumed to already contain only voxels from within a co-registered thoracic mask. Let (x_v, y_v) denote the spatial coordinates of each voxel $v \in \{1, \dots, V\}$. A *window* of radius r centred on voxel a is the index set

$$W(a; r) = \left\{ v \in \{1, \dots, V\} : (x_v - x_a)^2 + (y_v - y_a)^2 \leq r^2 \right\} = \{w_1, \dots, w_{|W|}\},$$

i.e. all voxels whose centre lies in the closed disc of radius r around (x_a, y_a) . Sliding the centre a successively through every voxel in the mask makes the window “move” across the lung. In this work we restrict windows to circular, in-plane neighbourhoods (Fig. 3.1), but other shapes or multi-slice extensions are possible in

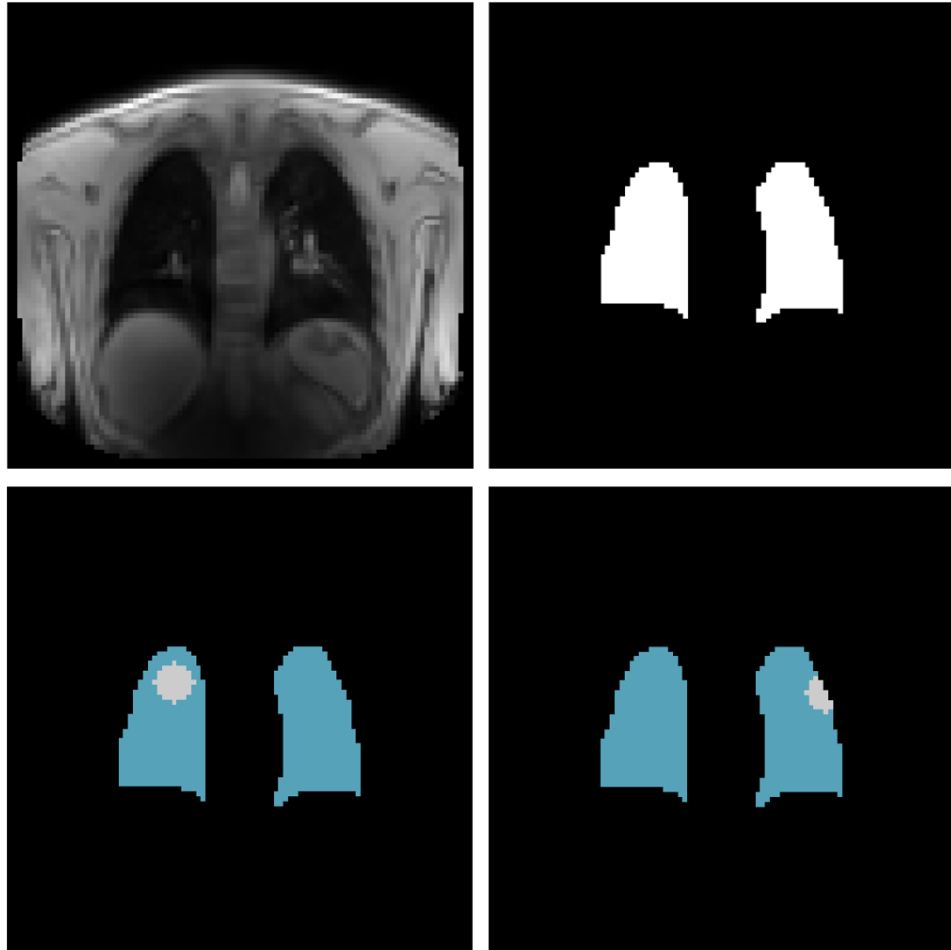


Figure 3.1: Top Left: Single dynamic from OE-MRI scan, Top Right: Manually segmented lung mask, Bottom Left: Sliding window (in white) with radius $r = 4$ at a particular location within lung mask. Note that the number of voxels in the window is not truncated as the window is sufficiently removed from the edges of the mask. Bottom Right: Sliding window with radius $r = 4$ at location along edge of mask. The number of voxels in the window gets truncated accordingly.

principle. The first row of Figure 3.1 shows a motion-registered dynamic in an OE-MRI scan of a healthy subject along the corresponding manually drawn lung-mask. The bottom row shows a window of radius $r = 4$ centred at two different voxels as it slides over the mask. For each centre voxel a and each chosen radius r , the idea of the present method is to form the time-series matrix

$$\mathbf{X}_{W(a;r)} = \begin{bmatrix} \mathbf{x}_{w_1,:} \\ \vdots \\ \mathbf{x}_{w_{|W(a;r)|},:} \end{bmatrix} \in \mathbb{R}^{|W(a;r)| \times T},$$

and to apply temporal ICA to $\mathbf{X}_{W(a;r)}$, thereby extracting one or more local oxygen-enhancement components. Later, all components generated from windows that included a given voxel will be aggregated to provide the voxel's final OE time-course.

3.2.2 Assumptions of the Method

As opposed to the assumption in [5] that all voxels share the same source signals, we make the more relaxed assumption here that the time course of each voxel $\mathbf{x}_{v,:}$ is composed of independent source signals specific to that voxel,

$$\mathbf{x}_{v,:} = \sum_{j=1}^{c_v} \alpha_j^{(v)} \mathbf{s}_{j,:}^{(v)}, \quad (3.1)$$

exactly one of which is an oxygen response. Hence, the matrix of time courses in each window may be written as

$$\bar{\mathbf{X}}_W = \bar{\mathbf{X}}_{\text{other}} + \bar{\mathbf{X}}_{\text{OE}}, \quad \mathbb{E}[\bar{\mathbf{X}}_{\text{OE}} \bar{\mathbf{X}}_{\text{other}}^\top] = \mathbf{0}, \quad (3.2)$$

where it is further assumed that each of the oxygen responses (rows in $\bar{\mathbf{X}}_{\text{OE}}$) is independent of all non-oxygen source mixtures in $\bar{\mathbf{X}}_{\text{other}}$. Whitening then gives

$$\mathbf{Z} = \mathbf{Z}_{\text{other}} + \mathbf{Z}_{\text{OE}}, \quad \mathbb{E}[\mathbf{Z}_{\text{OE}} \mathbf{Z}_{\text{other}}^\top] = \mathbf{0}, \quad (3.3)$$

where the c rows in \mathbf{Z}_{OE} maintain independence of the c rows in $\mathbf{Z}_{\text{other}}$. Under appropriate dimensionality c , temporal ICA is assumed to find a *single* vector $\mathbf{w}_i \in \mathbb{R}^c$ which isolates the oxygen responses, such that

$$\mathbf{s}_W^{OE} = \mathbf{w}_i^\top \mathbf{Z} = \mathbf{w}_i^\top \mathbf{Z}_{\text{other}} + \mathbf{w}_i^\top \mathbf{Z}_{\text{OE}} \approx \mathbf{w}_i^\top \mathbf{Z}_{\text{OE}}. \quad (3.4)$$

Hence, the recovered OE response is

$$\mathbf{s}_W^{OE} = \mathbf{w}_i^\top \mathbf{D}_{\parallel}^{-1/2} \mathbf{E}_{\parallel}^\top \bar{\mathbf{X}}_{\text{OE}}, \quad (3.5)$$

a mixture of the true oxygen responses $\mathbf{s}^{(v,OE)}$ in the window and (approximately) independent of every row in $\mathbf{X}_{\text{other}}$. When the oxygen response in voxel v is similar to that of other voxels in a given window, \mathbf{Z}_{OE} will encode that shared direction and \mathbf{s}_W^{OE} should be a good approximation of that response. Likewise the associated weight $(a_v^{OE})^2$, will be a good approximation of the variance in voxel v contributed by the oxygen response. On the other hand, when the response in voxel v differs significantly (and has a variance which does not dominate that of the other responses), its oxygen response will hardly be included in the rank c projection \mathbf{Z} and \mathbf{s}_W^{OE} will be a poor representation. The associated $(a_v^{OE})^2$ is then expected to be commensurately smaller. It follows that the weights a_v^{OE} are a means with which one may compare the representativeness for voxel v of OE components \mathbf{s}_W^{OE} extracted across different windows.

3.3 Exploring the Parameter Space

There are a number of ambiguities on how to apply temporal ICA in the sliding window. Here we discuss these ambiguities and how they will be explored in an initial experiment on an OE-MRI scan of a healthy individual. The scan in question was a dual echo spoiled gradient scan (using the sequence defined in [15]) carried out on a Philips Ingenia scanner (Philips Healthcare, Best, Netherlands) at 3.0T with temporal resolution of 1.5s and $TE_1 = 0.71\text{ms}$ and $TE_2 = 1.2\text{ms}$. Gas was delivered to the subject through a non-rebreathing face mask at a rate of 15 L/min. The subject commenced breathing medical air (21% O_2) and switching between medical air and 100% O_2 took place every 90s (i.e. after every 60 images) for a total of 630 seconds (420 images). It is the third (from a total of four) coronal slice from this scan and the associated manually segmented lung mask which is shown in Figure 3.1. The dynamics in the scan had already undergone motion registration to account for respiratory and cardiac motion. We shall refer to the series of images from the first echo of this scan as *Scan 1*.

3.3.1 Variation and The Number of Components

The dimensionality c chosen for ICA controls how much of the variance in the raw time-series matrix $\mathbf{X}_{W(a;r)}$ is retained. Too few dimensions c risks discarding the oxygen responses for some voxels entirely during projection to the whitened space. On the other hand, raising c captures more overall variance, but increases the risk that the oxygen response is split across multiple ICA components (i.e. the identification of multiple columns \mathbf{w}_i for which $\mathbf{w}_i^\top \mathbf{Z}_{\text{other}} \approx 0$), making it difficult to identify them. The number of retained dimensions therefore has a decisive influence on the resulting components, and even with the same dimensionality c , different random initialisations can lead to different decompositions.

Unless the number of independent sources is known exogenously, there is no general method by which to identify the optimal dimensionality c for use in ICA. In OE-MRI, however, we expect at least three independent processes governing the dynamics in each scan: the respiratory cycle, the cardiac cycle, and the oxygen-enhancement cycle (which we wish to identify). Furthermore, with FastICA, the possible number of dimensions c is bounded above by the number $|W(a;r)|$ of voxels in a window. In an initial experiment on *Scan 1* we therefore repeat temporal ICA in each window $W(a;r)$ with all possible dimensionalities $c \in \{3, \dots, |W(a;r)|\}$.

3.3.2 Initialising the ICA Algorithm

Another aspect of running FastICA within each window is the number of times that the algorithm is repeated for a given number of dimensions c . Due to the iterative nature of measuring negentropy based on "estimated realisations" of the variables S_i , the FastICA algorithm described previously can get stuck at sub-optimal local maxima. A common strategy to cope with this problem is to repeat the iterative algorithm with different initial guesses for the mixing matrix \mathbf{W} , and to identify clusters of the resulting components [23]. Given satisfactory stability within a cluster containing components of interest, a suitably defined average of that cluster may be extracted. In order to address the question of initialisation, the initial experiment on *Scan 1* used repeated temporal ICA with five different seeds for every dimensionality c .

sionality c in every window $W(a; r)$.

3.3.3 Identifying the oxygen-enhancement component

As in [5] we rank every extracted ICA component \mathbf{s} by its Spearman correlation with a set of synthetic "OE probes" $\{\mathbf{f}_n\}$. Direct spectral tests are unattractive as components are noisy and an individual scan seldom contains many full periods. Each \mathbf{f}_n is constant at a value of one before the first gas switch to O_2 at time point t_1 , and becomes a unit-variance sinusoid beginning n time-points later. We must use such functions for identification of the OE-component as we do not know its true shape, only that it should display some degree of periodicity at a known frequency due to the gas switching scheme. In [5], only a single reference curve \mathbf{f}_1 was used, with onset of the sinusoidal pattern in the time-step immediately after switching from medical air to oxygen. In this work, however, we note that because of different perfusion/diffusion delays throughout the lungs, a voxel v will react to the gas change at some delay $t_1 + n_v$. We will make an assumption that this delay stays fixed across switches from air to O_2 and vice versa. The different reference functions \mathbf{f}_n are designed to account for this potential delay in OE-response. Because the gas switching cycle alternates between O_2 and air every 60 samples (≈ 90 s) in *Scan 1*, any identifiable OE signal must start somewhere inside that 60-sample window; a latency longer than 60 could be falsely identified with the subsequent gas switch back to air, and its sign would be ambiguous. Hence, we pre-compute 60 possibilities ($\{\mathbf{f}_n\}$, $n = 0, 1, \dots, 59$), 15 of which are shown schematically in Fig. 3.2. For every extracted component \mathbf{s}_i , we use the largest absolute Spearman coefficient across reference functions \mathbf{f}_n :

$$\rho(\mathbf{s}_i) = \max_n |\rho_{\text{Spearman}}(\mathbf{s}_i, \mathbf{f}_n)|,$$

as a simple proxy for "how periodic" the component is at the switching frequency, irrespective of sign.

For each ICA run, we retain only the component with the greatest $\rho(\mathbf{s}_i)$ due to the assumption that for appropriate c , the oxygen response is (approximately)

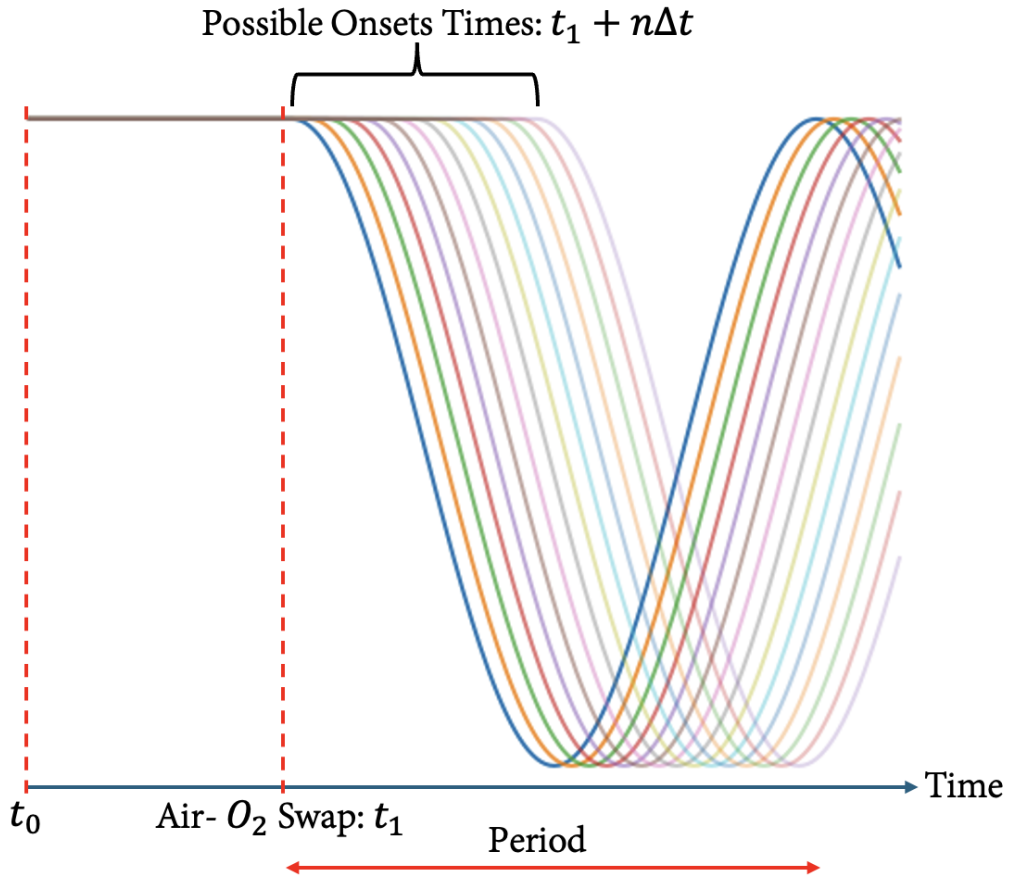


Figure 3.2: Fifteen reference functions are shown with transition to cyclic oscillations at some delay $n\Delta t$ after the first gas switch. For Scan 1, $t_1 = 90s$ and $\Delta t = 1.5s$. To avoid cluttering, further gas switches are not plotted, but in accordance with the shape of the reference functions, the first switch from O_2 to air would occur at a time Δt before the trough in the clear blue curve

isolated only by one column $\mathbf{w}_i \in \mathbf{W}$. This assumption is crucial as it would be infeasible to investigate the periodicity of all possible combinations of components and as it allows us to easily compare values of c . It is possible, however, that a range of values for c each produce a single component approximately associated with the OE responses.

3.3.4 Grouping Voxels on Different Scales

Windowed ICA extracts several OE components for a voxel v by embedding it in multiple neighbourhoods $W(a; r)$ containing roughly πr^2 surrounding voxels. Difficulties arise when only a small cluster of $m \ll \pi r^2$ voxels near v share the same OE

pattern or when the spatial distribution of those voxels means they never form a sufficient proportion of a window W . Any window that fully or partially captures this cluster will include many dissimilar voxels, and the oxygen response shapes of the majority may dominate so that the true response signal in v 's is entirely suppressed.

To mitigate this, we can analyse multiple window sizes. Smaller radii should reveal more local response shapes that larger windows might suppress during whitening. On the other hand, smaller windows are more susceptible to location-specific noise that can distort the extracted component. For the initial experiment on *Scan 1* we investigated the radii $r = 2, 3, 4$ (larger radii would render the exhaustive experiment intractable in terms of computational time).

3.3.5 Experiment Set-up & Computational Complexity

There were 871 voxels in the mask of *Scan 1* and 420 dynamics were acquired. For all radii $r = 2, 3, 4$, a window was slid across the lung mask shown in Figure 3.1, being centred at each voxel in the mask exactly once. In each window $W(a; r)$, temporal ICA was repeated on the matrix $\mathbf{X}_{W(a; r)}$ five times for each of the dimensionalities $c = 3, \dots, |W(a; r)|$ (i.e. a total of $5|W(a; r)|$ ICA runs for each window). The Spearman correlation against all 60 reference functions was calculated for each of the

$$5 \sum_{i=3}^{|W|} i = \frac{5(|W| - 2)(|W| + 3)}{2} \quad (3.6)$$

extracted components within each window. The computations were done in Python 3.11 on a MacBook Pro M1 with each ICA iteration calculated in parallel across 10 cores. Each call to `scikit-learn`'s FastICA was run in symmetric mode, with the default parameters of 200 Newton iterations and a logcosh contrast function.

As an illustration of the computational complexity, consider that for a window with radius 4 located such that all 49 voxels were inside the mask, $5 \times (49 - 2) = 235$ calls to fastICA had to be made to extract the relevant components. This amounted to

$$5 \sum_{i=3}^{49} i = \frac{5(49 - 2)(49 + 3)}{2} = 12,220 \quad (3.7)$$

components being extracted. Each component had to be checked against 60 ref-

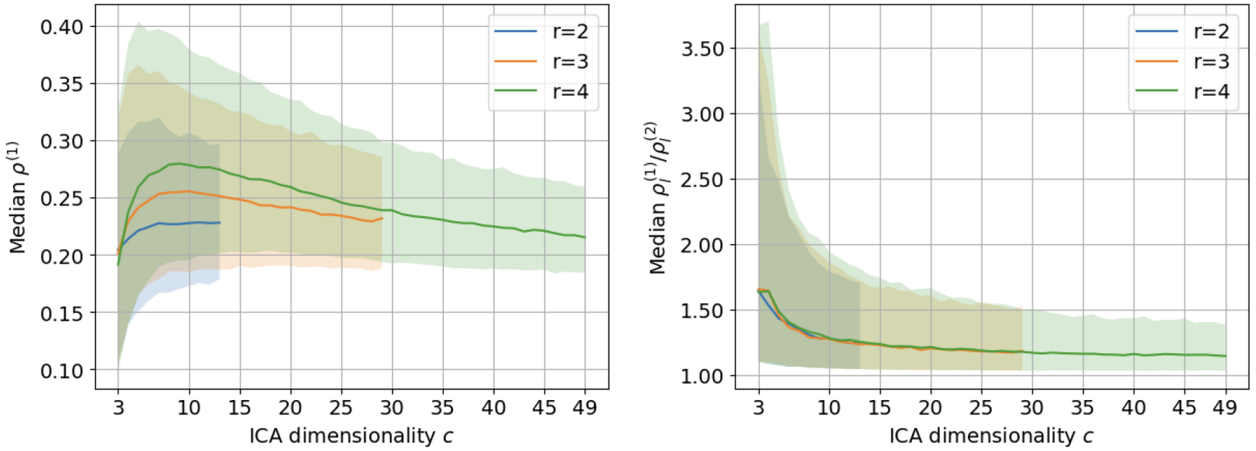


Figure 3.3: Experiment 1 Statistics. Left: Median of best Spearman correlation extracted from each run of ICA against dimensionality c , stratified by window radius. Hashed areas show the 10-90th percent interval. Right: Corresponding plot showing ratio of first to second-best Spearman correlation from each run of ICA.

erence functions, making for $60 \times 12220 = 733,200$ Spearman correlation calculations. Hence, for $r = 4$, to extract the OE-component at a single location among 871 (number of voxels in the mask), up to 235 calls to fastICA and 733,200 Spearman correlation calculations were necessary. The running time for this experiment was > 5 hours, and the majority of that time was spent doing the calculations for the window of radius $r = 4$. For this reason, larger radii were not considered.

3.3.6 Experiment 1: Results

Consider a window $W(a; r)$ on which ICA is repeatedly conducted with $c = 3, \dots, |W(a; r)|$ dimensions. Let $\rho(1, l, c)$ denote the best Spearman coefficient extracted from a particular run with dimensionality c , where l denotes the initialisation among the five tested. Accordingly, let $\rho(2, l, c)$ denote the second highest Spearman coefficient extracted from that run. The left panel in figure 3.3 shows the relationship between the median of all $\rho(1, l, c)$ and c across the 871 window locations, stratified by the radius r . The right panel shows the median of the corresponding ratios $\rho(1, l, c)/\rho(2, l, c)$. For every radius r , we note a general dependence of the $\rho(1, l, c)$ and the ratios $\rho(1, l, c)/\rho(2, l, c)$ on the dimensionality c used in ICA. In particular, the median among the best Spearman coefficients $\rho(1, l, c)$ for each di-

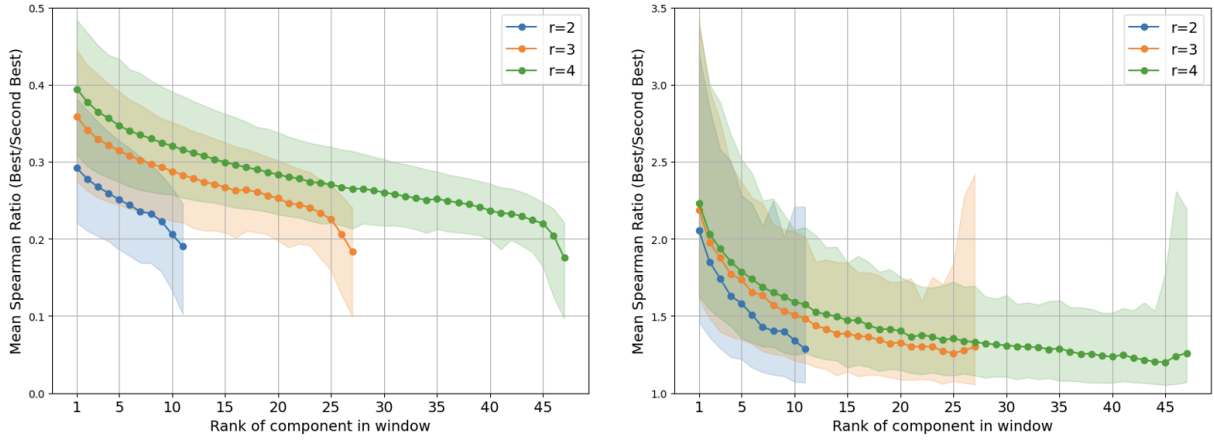


Figure 3.4: Experiment 1 Statistics. Left: In each window every dimensionality c receives a rank according to the best Spearman coefficient produced at with c dimensions. This plot is a rank-wise median of those scores over all windows. Hashed areas show 10th and 90th percentiles of the rank-wise Spearman correlations. Right: The equivalent plot (in particular according to the same ranking) for the ratio of best to second-best Spearman correlation from each ICA run. The tails show spikes in the 10th and 90th percentile due to the limited number of runs in which all 13, 29 and 49 dimensionalities could be tested (corresponding to radii 2,3,4).

dimensionality c appears to peak around $c = 10$. This suggests that, on average, the dimensionality at which ICA is best able to extract a periodic component similar to one of the reference functions is about 10. We note also that the ratio of Spearman coefficients of the best to second best component from each run is similar across radii and is highest for smaller dimensionalities c .

Now, for each window $W(a; r)$ and each dimensionality c , let $\rho(1, \hat{l}_c, c)$ denote the maximal coefficient extracted across the five initialisations. Let $R = \text{sort} \{ \rho(1, \hat{l}_c, c) : c \leq |W(a; r)| \}$ denote the descending list of such Spearman coefficients extracted from each window. The left panel in Figure 3.4 shows the median of each *rank* (i.e. index) in R across all windows. The plot contrasts the periodicity score of the single most periodic component (whatever its c) with the best-scoring components obtained at every other dimensionality. The right panel shows the medians of $\rho(1, \hat{l}_c, c)/\rho(2, \hat{l}_c, c)$, but according to the same ranking in terms of $\rho(1, \hat{l}_c, c)$. It may be noticed that there is no clear spike in the Spearman coefficient and corresponding ratio for the optimal dimensionality c (i.e. while it has the highest value,

there is no substantial "drop" in the median values of the plots between the first and second ranked positions).

The top panel of figure 3.5 shows the dimensionality c which produced the most periodic component when the sliding window of different radii was centred at each respective pixel. The middle panel shows the corresponding Spearman coefficient values, whereas the bottom panel shows the stability of the best Spearman coefficient with respect to the five different initialisations.

3.3.7 Experiment 1: Discussion

As mentioned in section 3.2.2, we are interested in ICA runs for which a single component satisfies $\mathbf{w}_i^\top \mathbf{Z}_{\text{other}} \approx 0$. As demonstrated in the right panel of 3.4, the best five ICA dimensionalities c produce Spearman ratios which in the median are above 1.5 for all radii (i.e. the component with the highest Spearman coefficient is at least 50% more periodic than the next one from the same run). We therefore conclude that the sliding window successfully identifies a single, most periodic component for "good" dimensionalities c .

If our procedure were accidentally tuned to a specific c , one would expect that dimensionality to exhibit an anomalously large Spearman (or Spearman-ratio) compared with the rest. The left panel in Figure 3.4 shows the opposite: when the components are ranked *across* dimensionalities, the median Spearman and its ratio decline smoothly with rank (there is no discontinuity or isolated spike). We note therefore that there is no naturally occurring threshold for the Spearman coefficient above which we can choose to retain the most periodic component for each dimensionality c . Hence, we have decided to design a scheme within which we retain only the most periodic component over all c and all initialisations.

3.3.8 Combining Components

Having determined the method by which to extract an OE-component from each window, we can then turn to the method of combining components for each voxel. Recall that every run of ICA gives a weight for each voxel-component pair. The weight squared is an estimate of the amount of variance in the raw timeseries of

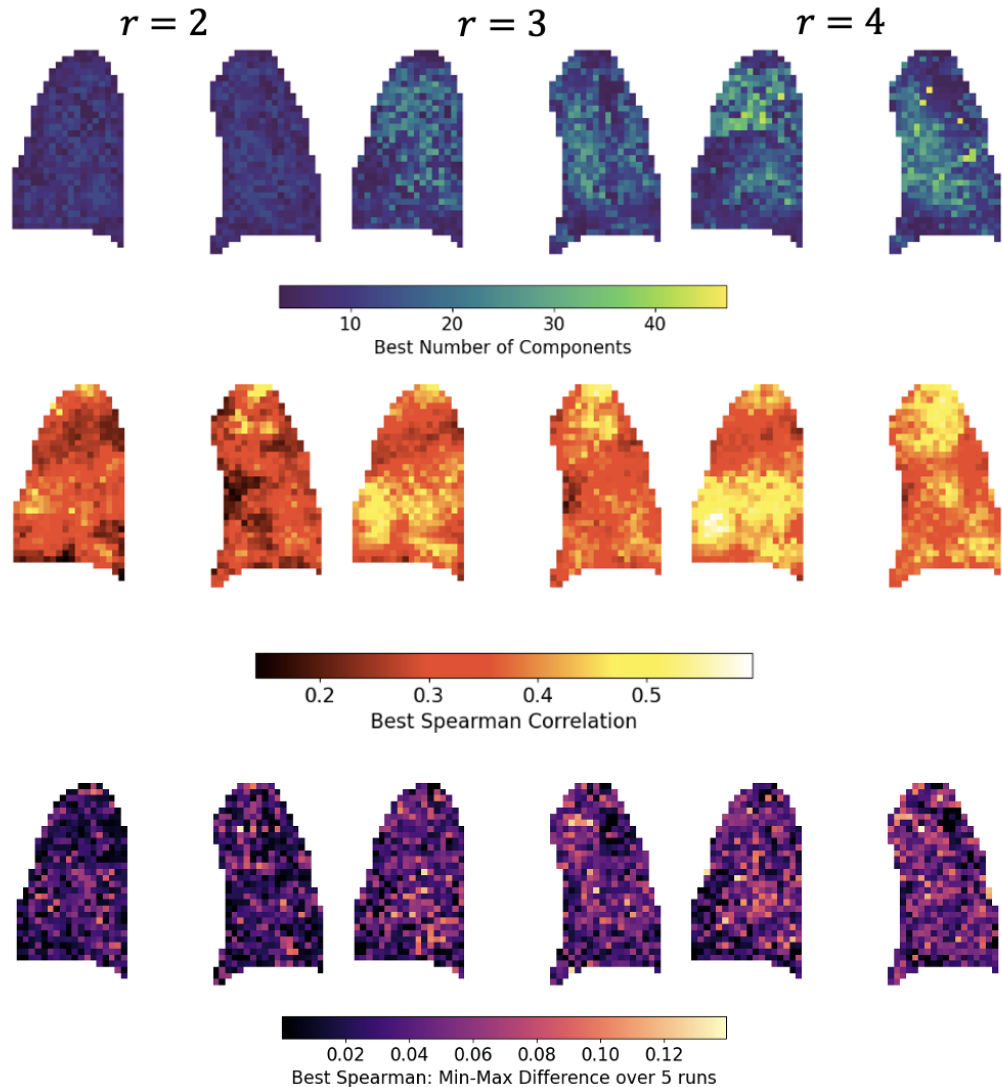


Figure 3.5: Statistics for Experiment 1. Each voxel a represents a property of the optimal component extracted in window $W(a; r)$ with radius r as indicated. Top: Dimensionality c leading to highest Spearman correlation; $\arg \max_c (\max_l \rho(1, l, c))$. Middle: Best Spearman correlation extracted in the window centred at each voxel; $\max_{l,c} \rho(1, l, c)$. Bottom: The stability to initialisation of the best Spearman coefficient across all dimensionalities; $\max_{l,c} \rho(1, l, c) - \min_l (\max_c \rho(1, l, c))$.

the voxel which may be explained by the component. We showed in section 3.2.2 that when an OE component can be extracted, it will be a weighted average of the oxygen responses within that window. To estimate the OE signal for a voxel covered by p overlapping windows we can therefore do a "variance"-weighted average

$$\mathbf{o}_v = \frac{1}{p} \sum_{k=1}^p (a_v^{\text{OE}})_k \mathbf{s}_k^{\text{OE}}, \quad (3.8)$$

so that windows with OE component similar to v (large $(a_v^{\text{OE}})_k$) dominate. Finally we store the mean normalised squared weight

$$\bar{a}_v^2 = \frac{1}{p} \sum_{k=1}^p \frac{(a_v^{\text{OE}})_k^2}{\text{Var}(\mathbf{x}_{v,:})}, \quad (3.9)$$

a single number that summarises how consistently and strongly the estimated OE responses explain the signal in voxel v .

3.4 Algorithm

Algorithm 3 shows the full implementation of the sliding window strategy. The algorithm is designed to take as input an MRI-scan along with a number of parameters. The parameters are the first switching time to O_2 from air, the period of the air- O_2 switching, the different window radii to be used about each individual voxel, the number of times ϵ the ICA pipeline is repeated for each location-radius-dimensionality combination, the number of reference functions with which to compare every extracted component, and the maximal number of dimensions c to consider in any ICA run.

3.4.1 Reducing the Computational Burden for Multiple Scans

For Experiment 1, it was noticed that the best component from 99.4% of ICA runs could be identified by comparing only with three reference functions whose onset of the cyclic response was delayed by time points 0, 20, 40, respectively (i.e. $\{\mathbf{f}_0, \mathbf{f}_{20}, \mathbf{f}_{40}\}$). For a component \mathbf{s}_i , the best Spearman correlation to one of these will not necessarily be the same as that produced by comparing to all 60 references

Algorithm 3 Extraction of OE-response per voxel

Require: Co-registered scan $\mathbf{X} \in \mathbb{R}^{V \times T}$, time point t_1 of first switch to O₂, period of air-O₂ switching scheme P , set of window radii $R \subset \mathbb{N}_+$, number of reference functions m , number of seeds per ICA run ε , maximal number of dimensions to use for ICA c_{\max} .

- 1: Construct reference block matrix $F \in \mathbb{R}^{m \times T}$. Let $\Delta_n = (n-1)\lfloor P/(2m) \rfloor$ denote the delay between gas switch and response in the n th reference function. Then

$$F_{n,t} = \begin{cases} 1, & 0 \leq t \leq t_1 + \Delta_n \\ \cos(2\pi(t - \Delta_n)/P), & t > t_1 + \Delta_n \end{cases} \quad (3.10)$$

```

2: Initialise for every voxel  $v$ :  $\mathbf{o}_v \leftarrow 0$ ,  $\bar{a}_v^2 \leftarrow 0$ ,  $ct_v \leftarrow 0$ 
3: for  $r \in R$  do ▷ Iterate over window radii
4:   for  $v = 1$  to  $V$  do ▷ Iterate over voxels/sliding window centres
5:      $\rho_{\max} \leftarrow 0$ ,  $\mathbf{p} \leftarrow \emptyset$ ,  $\mathbf{q} \leftarrow \emptyset$  ▷ Init. window coefficient, OE-component, and weights
6:     for  $c = 3$  to  $\min\{c_{\max}, |W(v;r)|\}$  do ▷ Iterate ICA dimensionalities
7:       for  $l = 1$  to  $\varepsilon$  do ▷ Iterate ICA initialisations
8:          $(\mathbf{S}, \mathbf{A}) \leftarrow \text{FastICA}(\mathbf{X}_{W(v;r)}, c, l)$ 
9:         for  $k = 1$  to  $c$  do ▷ Iterate over extracted ICs
10:          for  $n = 1$  to  $m$  do ▷ Iterate over reference functions with different delays
11:             $\rho \leftarrow \rho_{\text{Spearman}}(\mathbf{s}_{k,:}, F_{n,:})$ 
12:            if  $|\rho| > \rho_{\max}$  then ▷ If Spearman coef. exceeds window's previous best
13:               $\rho_{\max} \leftarrow |\rho|$ ,  $\mathbf{p} \leftarrow \mathbf{s}_{k,:}$ ,  $\mathbf{q} \leftarrow \mathbf{a}_{:,k}$  ▷ Get IC and weights
14:            end if
15:          end for
16:        end for
17:      end for
18:    end for
19:    for all  $w_i \in W(v;r)$  do ▷ Add to running sums of voxels in window
20:       $\mathbf{o}_{w_i} \leftarrow \mathbf{o}_{w_i} + q_i \mathbf{p}$ ,  $\bar{a}_{w_i}^2 \leftarrow \bar{a}_{w_i}^2 + q_i^2 / \text{Var}(\mathbf{x}_{w_i,:})$ ,  $ct_{w_i} \leftarrow ct_{w_i} + 1$ 
21:    end for
22:  end for
23: end for
24: for  $v = 1$  to  $V$  do ▷ final averaging
25:    $\mathbf{o}_v \leftarrow \mathbf{o}_v / ct_v$ ,  $\bar{a}_v^2 \leftarrow \bar{a}_v^2 / ct_v$ 
26: end for
```

\mathbf{f}_n . However, it is more important whether a comparison only with these three references would maintain transitivity between the components identified as best by each dimensionality c used within a window. To reduce the computational burden, we are interested in the impact of using only these three reference functions.

Note further the high degree of uniformity, relative to optimal Spearman mag-

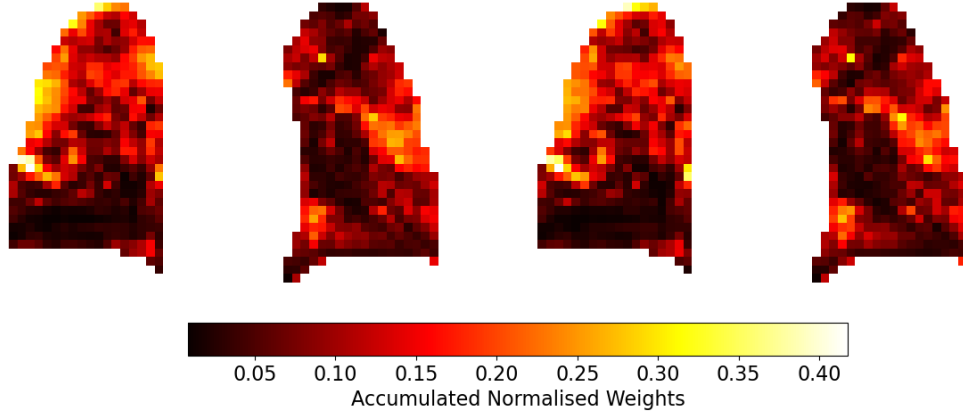


Figure 3.6: Weights \bar{a}_v^2 in each voxel from Algorithm 3 applied to *Scan 1* first with $m = 60$, $\epsilon = 5$, $c_{\max} = \infty$ and then with $m = 3$, $\epsilon = 1$, $c_{\max} = 40$. For both runs $R = \{2, 3, 4\}$.

nitude, across initialisations in each window as indicated by the middle and bottom panels of Figure 3.5. It is obvious that the computational complexity of Algorithm 3 grows linearly with ϵ . We are therefore interested in the impact of reducing ϵ on the final estimated oxygen responses \mathbf{o}_v in each voxel.

Finally, we note that for $r = 4$, 95% of windows produced a component generated from an ICA $c < 30$ (the window size for $r = 2, 3$ never exceeds 30). The fastICA algorithm increases in complexity for increasing c and larger c means more components have to be compared to the reference functions. Hence, we are interested in the stability of the pipeline's outcome when the maximal number of components is restricted.

In line with Experiment 1, we first applied Algorithm 3 to *Scan 1* with $m = 60$, $\epsilon = 5$, $c_{\max} = \infty$ (in practice the maximal number of dimensions that can be considered in a window corresponds to the number of voxels in the window). The algorithm was then applied with $m = 3$ (i.e. the delays 0, 20, and 40), $\epsilon = 1$, $c_{\max} = 40$. In both cases the set of radii was $R = \{2, 3, 4\}$. Figure 3.6 shows the weight maps produced by the two runs of Algorithm 3 applied to *Scan 1*. Figure 3.7 shows the Pearson correlation calculated between the two time series generated for each voxel. The weight maps are almost indistinguishable and we note the high degree

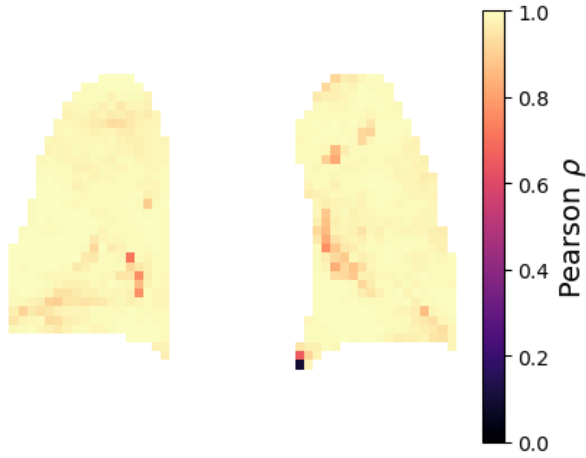


Figure 3.7: Pearson correlation between estimated oxygen responses $\mathbf{o}_v^{(1)}$ and $\mathbf{o}_v^{(2)}$ as produced from Algorithm 3 applied to *Scan 1* first with $m = 60$, $\epsilon = 5$, $c_{\max} = \infty$ and then with $m = 3$, $\epsilon = 1$, $c_{\max} = 40$. For both runs $R = \{2, 3, 4\}$.

of agreement between the shapes of the voxel-wise aggregated time series. The median (Pearson) correlation coefficient is 0.987 with the 5th and 95th percentiles being 0.935 and 0.996, respectively. The only correlation coefficients below a value of 0.7 are at an edge of the mask (bottom left corner in left lung, Figure 3.7), where the quality of any parenchymal segmentation may be inaccurate, such that no oxygen response could be detected. We can therefore say with a high degree of certainty that making the above simplifications are justified for the relevant slice of *Scan 1*. These simplifications reduced computational time for the given slice from > 5 hours to ≈ 15 minutes on the system used in this work. In applying Algorithm 3 to other OE-MRI scans, we will also apply Algorithm 3 with $m = 3$, $\epsilon = 1$, $c_{\max} = 40$. While we cannot be certain of the exact impact of these simplifications for other scans, it is a necessary adjustment to make computational times practical.

Chapter 4

Modelling

Having obtained estimates for the oxygen response in each voxel of a scan, we are generally interested in the parameters characterising these time courses. In [4], a number of piecewise constant, piecewise linear, and piecewise exponential functions were used to fit the raw time series of each voxel in an OE-MRI scan. A similar strategy was followed in [19, 15, 18], albeit using only the piecewise exponential function.

In this work, four piecewise exponential target functions and two linear references are used to fit the estimated OE-components for each of 17 scans, seven of which were of healthy subjects and ten of which were of long COVID patients. Two of the target functions correspond to models tested in [4]. The other two piecewise-exponential models tested are extensions to these models. The subjects were all scanned on a Philips Ingenia MRI scanner at 3.T with the same sequence specifications and gas switching scheme as *Scan 1*. Four coronal slices at different depths were acquired at each time point for each subject. We use only the images generated by the set of first echoes for each scan.

4.1 Model Functions

We describe first the most complex piecewise exponential which will be considered here. The other three are sub-models of this. We use piecewise exponential functions as these are the ones that have been applied to OE-MRI data with the greatest success in the literature [4, 15, 18, 19].

Consider an OE-MRI scan with the first switch to 100% O_2 at t_1 and period of $P \in \mathbb{N}$ of the air-oxygen switching scheme (with a switch every $P/2$ time steps). Further, assume that some voxel only reacts to a gas switch at some (integer) delay in time steps Δt . We define

$$k(t, \Delta t) = \left\lfloor \frac{t - (t_1 + \Delta t)}{P/2} \right\rfloor \quad h(t, \Delta t) = t - (t_1 + \Delta t) - \frac{P \times k(t, \Delta t)}{2}. \quad (4.1)$$

The integer $k(t, \Delta t)$ tells us what gas response lobe we are currently in; it is even if we are currently in a lobe of O_2 wash-in and odd if we are in a period of O_2 wash-out. The function $h(t, \Delta t)$ simply describes the number of time steps since the start of the current lobe. Then, let

$$g(t, \tau) = 2 \exp(-t/\tau) - 1 \quad (4.2)$$

model the exponential evolution of the OE-response during a lobe of oxygen wash-in or wash-out, where τ is a curvature parameter. If the OE-response is S at the start of a lobe, then after a time $t' < P/2$, its value becomes $g(t', \tau) \cdot S$. In particular, after a full oxygen wash-in lobe of duration $P/2$, the OE-response value has changed to $G_{\text{in}}S$, where $G_{\text{in}} = g(P/2, \tau_{\text{in}})$. At the end of the following wash-out lobe, the OE-response value has changed to $G_{\text{out}}G_{\text{in}}S$, where $G_{\text{out}} = g(P/2, \tau_{\text{out}})$.

For the parameters $\theta_4 = (\alpha, \beta, \Delta S, \Delta t, \tau_{\text{in}}, \tau_{\text{out}})$, the most complex piecewise exponential function f_4 to which we wish to fit the OE-response is then

$$f_4(t; \theta_4) = \begin{cases} \Delta S + \alpha, & t \leq t_1 + \Delta t \\ \Delta S G_{\text{in}}^{\frac{k(t, \Delta t)}{2}} G_{\text{out}}^{\frac{k(t, \Delta t)}{2}} g(h(t, \Delta t), \tau_{\text{in}}) + \beta(t - t_1 + \Delta t) + \alpha, & \substack{t > t_1 + \Delta t \\ k(t, \Delta t) \text{ even}} \\ \Delta S G_{\text{in}}^{\frac{k(t, \Delta t)+2}{2}} G_{\text{out}}^{\frac{k(t, \Delta t)}{2}} g(h(t, \Delta t), \tau_{\text{out}}) + \beta(t - t_1 + \Delta t) + \alpha, & \substack{t > t_1 + \Delta t \\ k(t, \Delta t) \text{ odd}} \end{cases} \quad (4.3)$$

The linear growth term β describes any linear drift in the OE-response signal, whereas α is simply a vertical shift. The other exponential models $f_1(t; \theta_1)$,

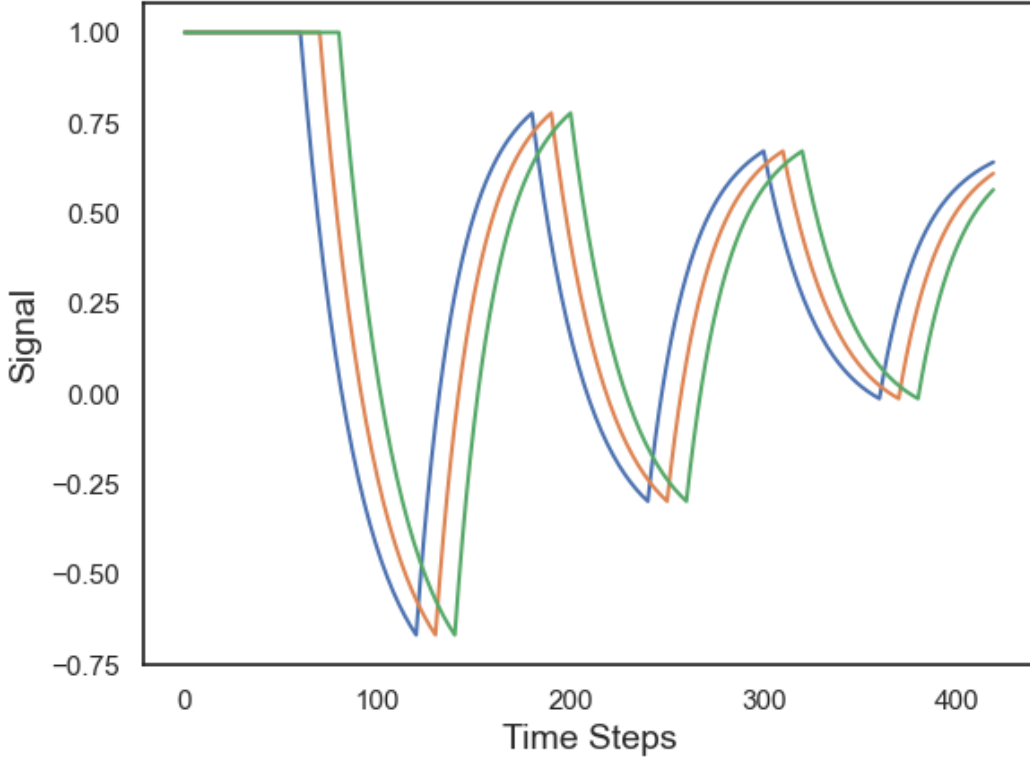


Figure 4.1: Three examples of the most complex piecewise exponential function f_4 for $\theta = (0, 0.001, 1, \Delta t, 30, 20)$, $t_1 = 60$, $P = 120$, and different delays $\Delta t = 0, 10, 20$.

$f_2(t; \theta_2)$, and $f_3(t; \theta_3)$ may then be described quite simply as

$$f_1(t; \theta_1) = f_1(t; \alpha, \Delta S, \Delta t, \tau) = f_4(t; \alpha, 0, \Delta S, \Delta t, \tau, \tau) \quad (4.4)$$

$$f_2(t; \theta_2) = f_2(t; \alpha, \Delta S, \Delta t, \tau_{\text{in}}, \tau_{\text{out}}) = f_4(t; \alpha, 0, \Delta S, \Delta t, \tau_{\text{in}}, \tau_{\text{out}}) \quad (4.5)$$

$$f_3(t; \theta_3) = f_3(t; \alpha, \beta, \Delta S, \Delta t, \tau) = f_4(t; \alpha, \beta, \Delta S, \Delta t, \tau, \tau) \quad (4.6)$$

Figure 4.1 shows an example of f_4 for $\theta = (0, 0.001, 1, \Delta t, 30, 20)$, $t_1 = 60$, $P = 120$, and different delays $\Delta t = 0, 10, 20$. Finally, we consider also the linear models

$$f_5(\alpha) = \alpha \quad \text{and} \quad f_6(\alpha, \Delta t, \beta) = \begin{cases} \alpha, & t \leq t_1 + \Delta t \\ \alpha + \beta(t - (t_1 + \Delta t)), & t > t_1 + \Delta t. \end{cases} \quad (4.7)$$

Models f_5 and f_6 are used as references to account for any voxels that did not show an OE-response or which demonstrated a drift across the scan, possibly induced by

the cumulative effects of O_2 inhalation or unrelated thermal effects.

4.2 Fitting

Algorithm 3 was applied to all slices and the first echo in each of the registered scans of seven healthy- and ten long COVID subjects. The algorithm was applied with $m = 3$ reference functions, three radii $R = 2, 3, 4$, a maximum ICA dimensionality $c_{\max} = 40$, and one initialisation $\epsilon = 1$ for each location-radius-dimensionality combination. The estimated OE-timeseries for each voxel (and in all slices) was then fitted to each of the functions $f_1, f_2, f_3, f_4, f_5, f_6$. In order to compare the present method to the "raw" voxel time series fits used in [19, 15, 17, 4], the same functions are also fitted to the raw, registered time series of each voxel.

The results in every voxel were fitted to each of the functions f_q by means of `curve_fit` from `scipy.optimize`. The bounds and initial values for each variable are as in table 4.1. It is easily seen that the provided model functions

	τ_{in}	τ_{out}	τ	α	ΔS	β
Init.	44.1	37.7	40.9	0	1	0
Bounds	(0.15, 90)	(0.15, 90)	(0.15, 90)	($-\infty, \infty$)	($-\infty, \infty$)	($-\infty, \infty$)

Table 4.1: Initial values and optimisation bounds used in voxel-wise fitting

f_2, f_3, f_4, f_5, f_6 are not differentiable with respect to the delay parameter Δt . Therefore, in models 2-6 all other parameters had to be optimised by means of an expensive grid search over the values $\Delta t = 0, \dots, 59$.

After fitting, the corrected Akaike information criterion was calculated for each model to compare performance within each voxel:

$$\text{AICc} = T \ln \left(\frac{1}{T} \sum_{i=1}^T (\mathbf{x}_i - f_q(t_i; \hat{\theta}^{(q)})) \right) + 2k_q + \frac{2k_q^2 + 2k_q}{T - k_q - 1}, \quad (4.8)$$

where \mathbf{x} is the registered time series or ICA-estimated OE response in the voxel, $\hat{\theta}^{(q)}$ are the optimised parameters for the particular model in the voxel, and k_q are the number of free parameters in the model. For each voxel, we retain the parameters of the model with the smallest AICc . We follow this individual approach for

each voxel as there is no reason to believe that the same oxygen response shape is followed in every region of the lung. Only voxels with superior Akaike coefficient for f_1, f_2, f_3, f_4 are considered oxygen-activated.

Due to the nested nature of the piecewise exponential model, we assign $\tau_{\text{in}}^{(q)} = \tau_{\text{out}}^{(q)} = \tau^{(q)}$ in cases where models f_1 or f_3 have the lowest AICc.

4.3 Testing for Differences Between Cohorts

Let μ_i denote the mean of parameter w over the oxygen-activated voxels for subject i . For each cohort, we compute the cohort-level summary statistic as the mean of these subject-level means:

$$\bar{\mu}_{\text{COVID}} = \frac{1}{10} \sum_{i \in \text{COVID}} \mu_i, \quad \bar{\mu}_{\text{Healthy}} = \frac{1}{7} \sum_{i \in \text{Healthy}} \mu_i.$$

We test the hypotheses

$$H_0 : \mathbb{E}[\mu | \text{COVID}] = \mathbb{E}[\mu | \text{Healthy}], \quad H_1 : \mathbb{E}[\mu | \text{COVID}] \neq \mathbb{E}[\mu | \text{Healthy}],$$

by first estimating the observed difference $\Delta_{\text{obs}} = \bar{\mu}_{\text{COVID}} - \bar{\mu}_{\text{Healthy}}$. We assess the uncertainty of Δ_{obs} via hierarchical bootstrap resampling with $B = 100,000$ bootstrap iterations, in which subjects are resampled with replacement within each cohort and a new cohort-level mean of subject-level means is computed. The resulting bootstrap distribution of Δ is used to obtain a central 95% confidence interval. The null hypothesis is rejected if this confidence interval does not include zero.

4.4 Results

4.4.1 ICA weights

Figure 4.2 shows first the normalised and accumulated weights in each voxel v in the third slice (counted anterior to posterior) of each scan. As a reminder, these weights are generated directly by Algorithm 3 and are an estimate of the total variance in the voxel attributable to the oxygen response. Figure 4.3 then shows the mean empirical cumulative density functions (ECDFs) of the weight in the healthy and long COVID

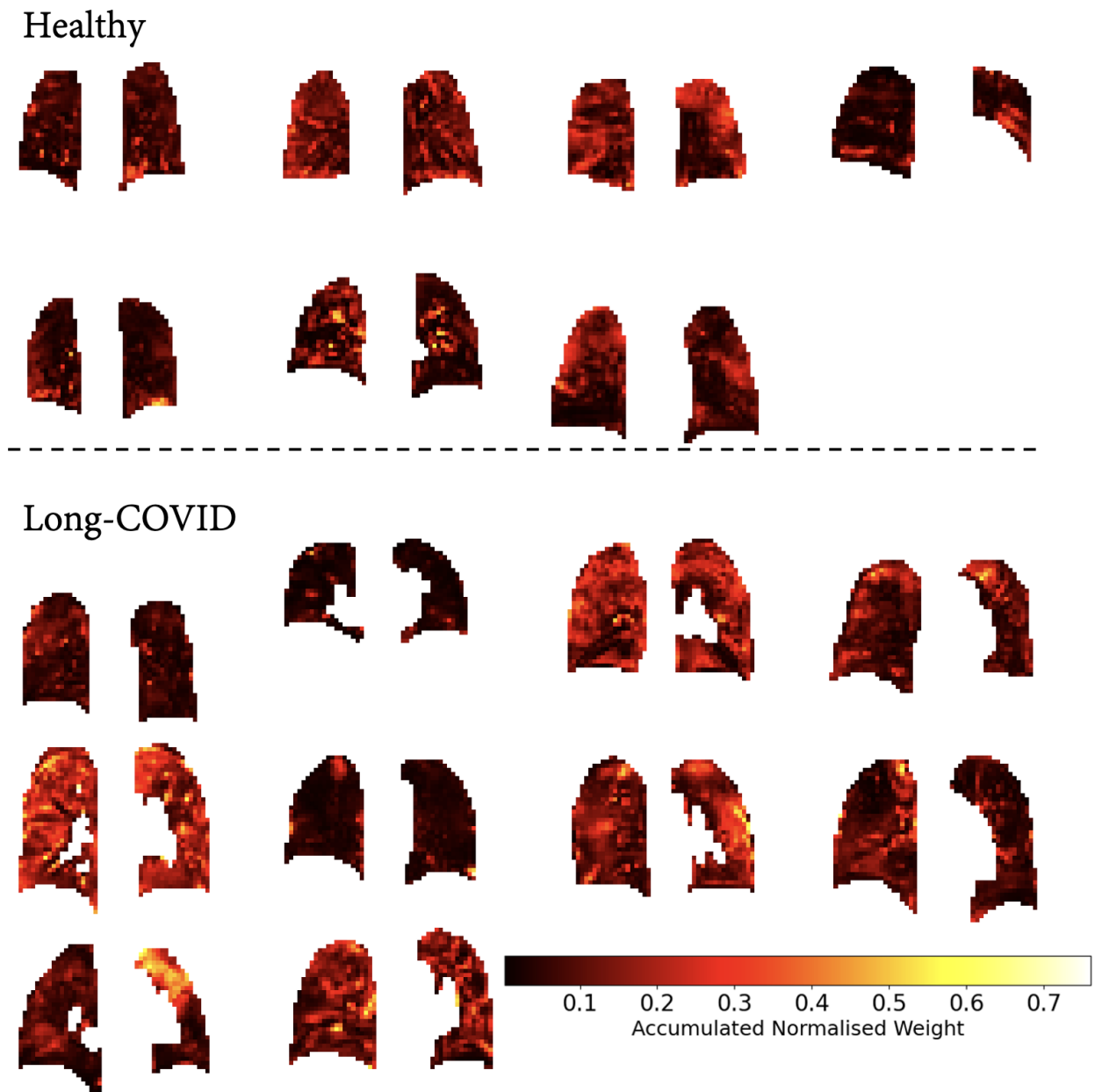


Figure 4.2: Weights \bar{a}_v^2 in each voxel from Algorithm 3 applied to the healthy and long COVID cohorts, respectively. Note that all slices have been placed on the same intensity scale, which is the reason *Scan 1* (the last of the slices in the healthy cohort) appears slightly dim compared to Figure 3.6.

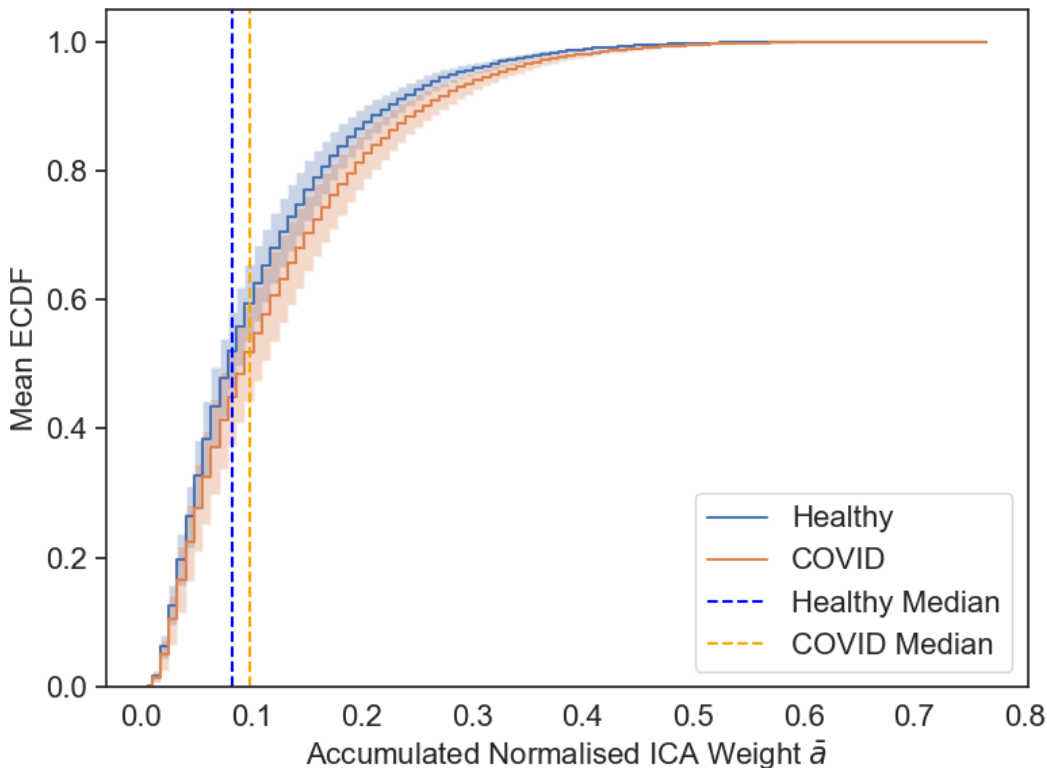


Figure 4.3: Mean empirical cumulative density function (ECDF) for the weights for the healthy and long COVID cohorts. Empirical CDFs are generated for each subject (using 100 bins) and then averaged at each weight level. The hashed areas show the standard error of the mean ECDF for each cohort. Vertical lines show the median weight for each cohort as estimated from the mean ECDF.

scans, respectively. The mean ECDF was calculated for each cohort by taking the mean of the ECDF of each subject within the cohort. When generating the ECDF for a subject, voxels from all slices are considered part of the same sample. This gives each subject equal importance within each cohort (calculating instead the overall ECDF of all voxels over an entire cohort would be skewed toward "larger" lungs). The shaded areas show the standard error of the mean at each value. We also show the median weight calculated from the mean ECDFs.

At this point it must be emphasised that the trapezoidal/midpoint numerical integral of the difference between mean healthy and COVID ECDFs *equals* the negative difference in sample mean of means we are interested in (in the limit where every voxel value gets a separate bin). In other words, the mean of means can easily be interpreted in terms of the empirical distribution, which is a significant advantage.

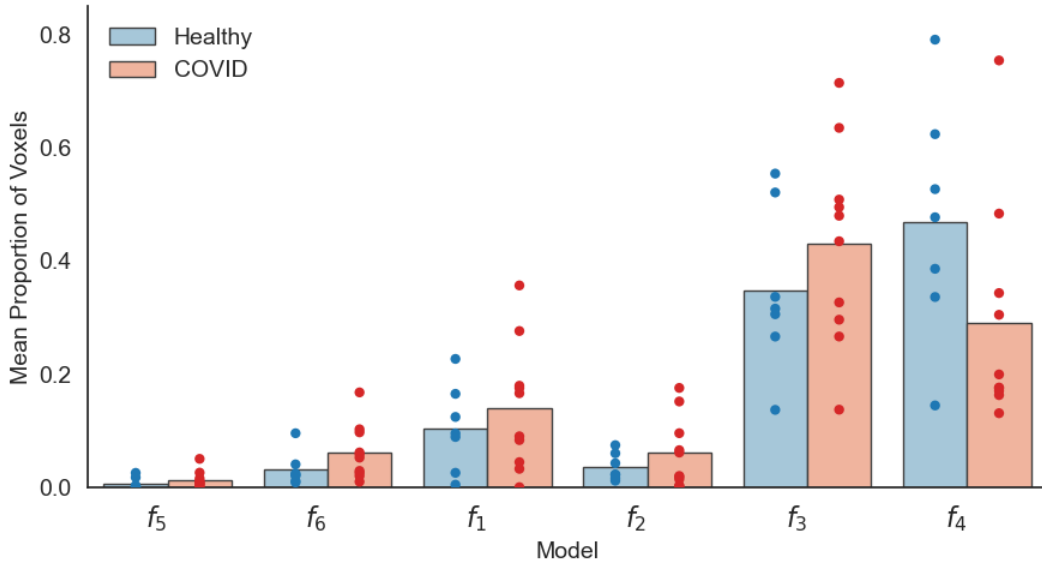


Figure 4.4: Proportion of voxels for which each model produced the best AICc score when fitted to the oxygen responses estimated by Algorithm 3, stratified by cohort. Bars correspond to the average proportion across scans, while the points correspond to proportions within individual scans.

In the case of the ICA weights in Figure 4.2, we find a CI of $[-0.0496, 0.0177]$. Thus, the 95% bootstrap CI for the signed difference between cohort means of means includes zero, so we do not find evidence of a distributional difference in weights between cohorts at the 5% level.

4.4.2 Model Distributions

Figure 4.4 shows the proportion of voxels, in each cohort, for which each model provided the best AIC when fitted to the oxygen responses estimated by Algorithm 3. Figure 4.5 shows the corresponding proportions for the models fitted to the raw data. The average proportions across scans (bars) are shown along with the proportions in individual scans (points). Across all slices in healthy-subject scans, the fraction of oxygen-activated voxels was

$$\hat{p}_{\text{Healthy}}^{\text{OA}} = \begin{cases} 0.96, & (\text{ICA data}) \\ 0.66, & (\text{raw data}) \end{cases}$$

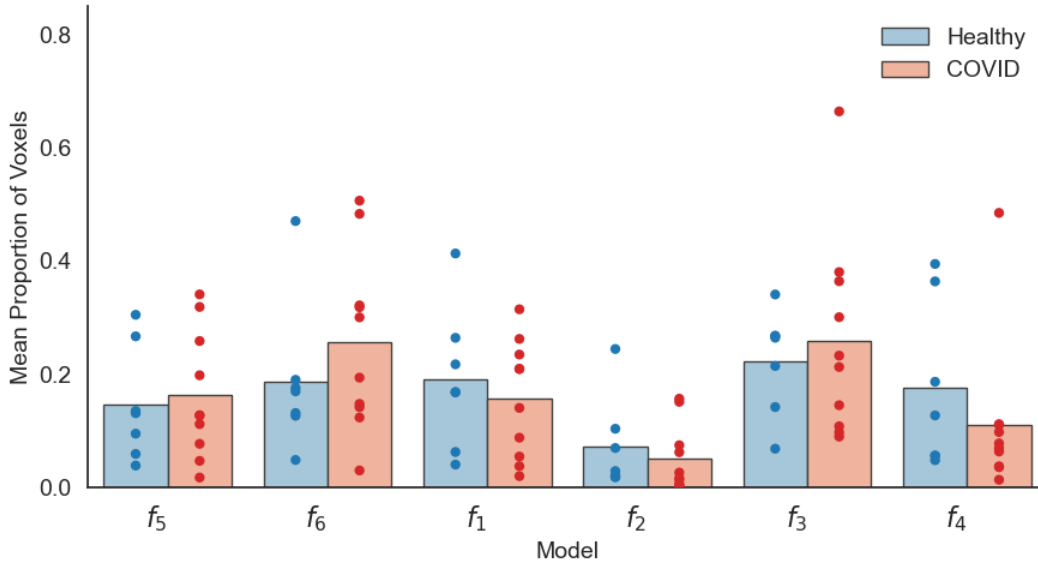


Figure 4.5: Proportion of voxels for which each model produced the best AICc score when fitted to the raw (registered) time series, stratified by cohort. Bars correspond to the average proportion across scans, while the points correspond to proportions within individual scans.

and for long COVID scans

$$\hat{p}_{\text{COVID}}^{\text{OA}} = \begin{cases} 0.92, & (\text{ICA data}) \\ 0.58, & (\text{raw data}) . \end{cases}$$

We then tested

$$H_0 : p_{\text{Healthy}}^{\text{OA}} = p_{\text{COVID}}^{\text{OA}} \quad \text{versus} \quad H_1 : p_{\text{Healthy}}^{\text{OA}} \neq p_{\text{COVID}}^{\text{OA}}$$

using a nonparametric (permutation) test. The two-sided p -values (i.e. the proportion of permutations for which $|p_{\text{Healthy}}^{\text{OA}} - p_{\text{COVID}}^{\text{OA}}| > \hat{p}_{\text{Healthy}}^{\text{OA}} - \hat{p}_{\text{COVID}}^{\text{OA}}$) were

$$p_{\text{ICA}} = 0.1244, \quad p_{\text{raw}} = 0.3406,$$

so in neither case can we reject H_0 at the 5% level.

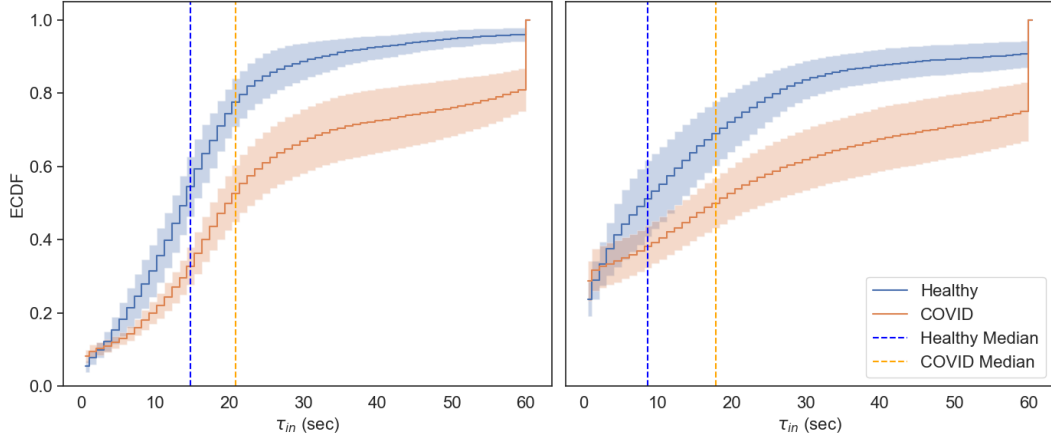


Figure 4.6: **Right:** Mean ECDFs for wash-in parameter τ_{in} in oxygen-activated voxels as found with fits to the time series from Algorithm 3 **Left:** Equivalent plots for fits to raw time series. For both figures, 60 bins were used for the ECDF.

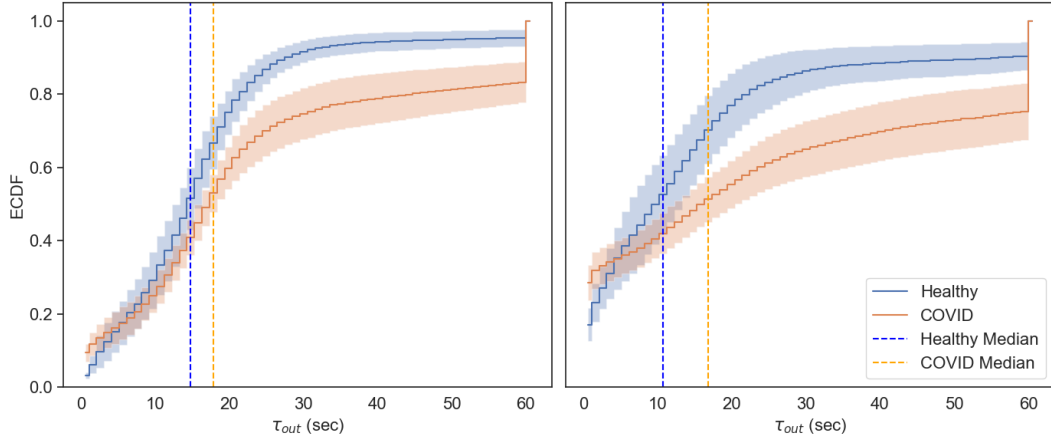


Figure 4.7: **Right:** Mean ECDFs for wash-out parameter τ_{out} in oxygen-activated voxels as found with fits to the time series from Algorithm 3 **Left:** Equivalent plots for fits to raw time series. For both figures, 60 bins were used for the ECDF.

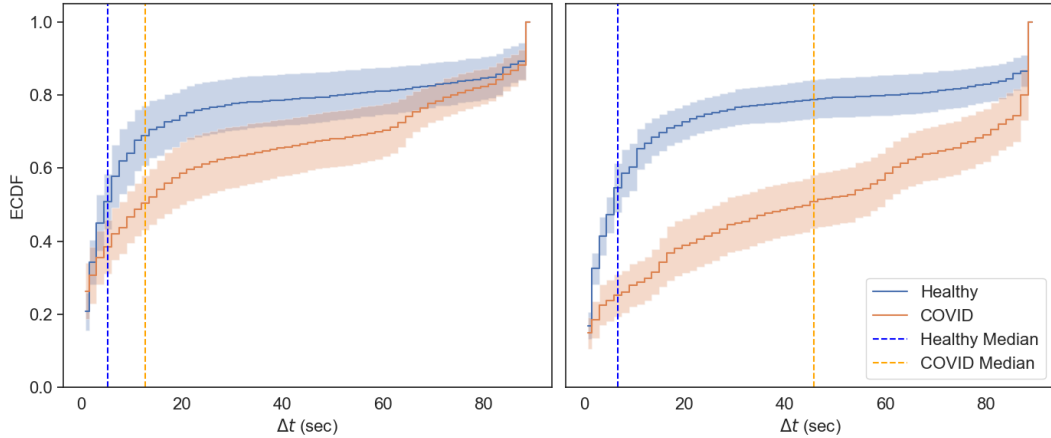


Figure 4.8: **Right:** Mean ECDFs for delay parameter Δt in oxygen-activated voxels as found with fits to the time series from Algorithm 3 **Left:** Equivalent plots for fits to raw time series. For both figures, 60 bins were used for the ECDF.

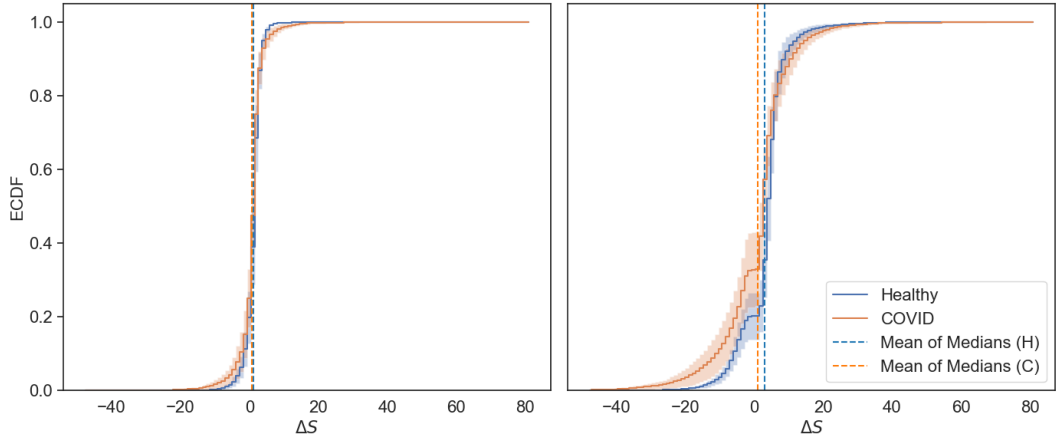


Figure 4.9: Right: Mean ECDFs for oxygen response scale parameter ΔS in oxygen-activated voxels as found with fits to the time series from Algorithm 3 **Left:** Equivalent plots for fits to raw time series. For both figures, 120 bins were used for the ECDF.

4.4.3 Parameter Estimates

In general, we are interested in interrogating the parameters τ_{in} , τ_{out} , Δt , and ΔS which are associated with the cyclic oxygen response. The parameters α and β are scale and drift parameters which cannot directly be associated with the oxygen response. Figure 4.6-4.10 shows the mean ECDFs for each of the parameters τ_{in} , τ_{out} , Δt , ΔS in the oxygen-activated voxels in each cohort and for the ICA-data and the raw fits. Data from all coronal slices is used. Parameter values have been converted to seconds where relevant. Figures 4.11 and 4.12 show the estimated wash-in time τ_{in} in slice three for both cohorts when calculated using the OE components from Algorithm 3 and the raw voxel-wise time series, respectively. Black voxels are those that are not oxygen-activated. Similar plots for the wash-out τ_{out} and the delay in any oxygen response Δt are shown in Figures 1-4 in appendix A. In the oxygen-activated cells, we use the bootstrapped CI for the differences in mean of means to assess whether there is a statistically significant difference between cohorts in terms of the parameters τ_{in} , τ_{out} , Δt , $|\Delta S|$. We also test for any difference in the adjusted coefficient of determination, \bar{R}^2 , of the optimal model in each voxel. Table 4.2 shows the estimated confidence intervals for the difference $\mathbb{E}[\mu | \text{COVID}] - \mathbb{E}[\mu | \text{Healthy}]$. The wash-in τ_{in} and wash-out τ_{out} rates in oxygen-activated voxels resulting from the present method is found to be significantly higher

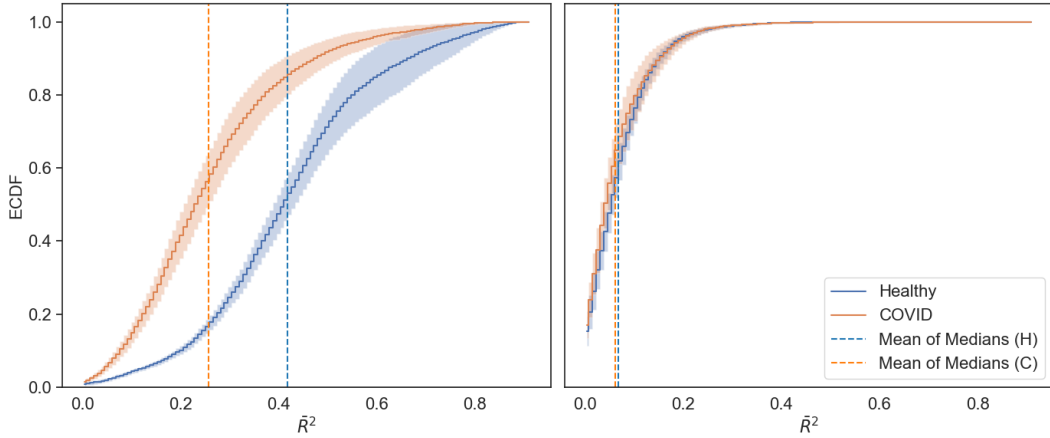


Figure 4.10: Right: Mean ECDFs for coefficient of determination \bar{R}^2 when comparing estimated oxygen responses from ICA method with optimal fitted function (among $f_1 - f_6$). **Left:** Equivalent ECDFs estimated using raw time series. In both cases 120 bins were used to generate the ECDFs.

Data / Param.	τ_{in}	τ_{out}	Δt	$ \Delta S $	\bar{R}^2
ICA	[3.07, 18.35]*	[1.30, 13.35]*	[-3.51, 15.65]	[-0.40, 1.28]	[-0.24, -0.09]*
Raw	[0.06, 20.89]*	[-0.47, 19.36]	[6.51, 23.08]*	[-0.88, 3.85]	[-0.03, 0.02]

Table 4.2: Bootstrapped confidence intervals for the difference $\mathbb{E}[\mu | \text{COVID}] - \mathbb{E}[\mu | \text{Healthy}]$ in cohort-wise mean of means of different parameters fitted on the estimated oxygen responses using the ICA model (Algorithm 3) and the raw time series. An asterisk denotes that we reject the null hypothesis of no significant difference at the 5% significance level.

in the healthy cohort than in the long COVID cohort at the 5% significance level. A significant difference was present for the wash-in but not for the wash-out when fitted on the raw time series. Conversely, no significant difference could be found at the 5% significance with the present method when examining the delay in oxygen response Δt . However, a significant difference was found for that parameter using the raw fits. No significant difference was found with either method for the magnitude of oxygen response ΔS , whereas only the present method using sliding window ICA found a significant difference in the adjusted coefficient of determination \bar{R}^2 .

A subtle point is the large disparity in the number of voxels marked as oxygen activated for the two data sets; as noted 96% (healthy) and 92% (long COVID) of voxels were marked as activated given the estimated OE responses from Algorithm 3, while the corresponding numbers for the raw time series were 66% and 58%.

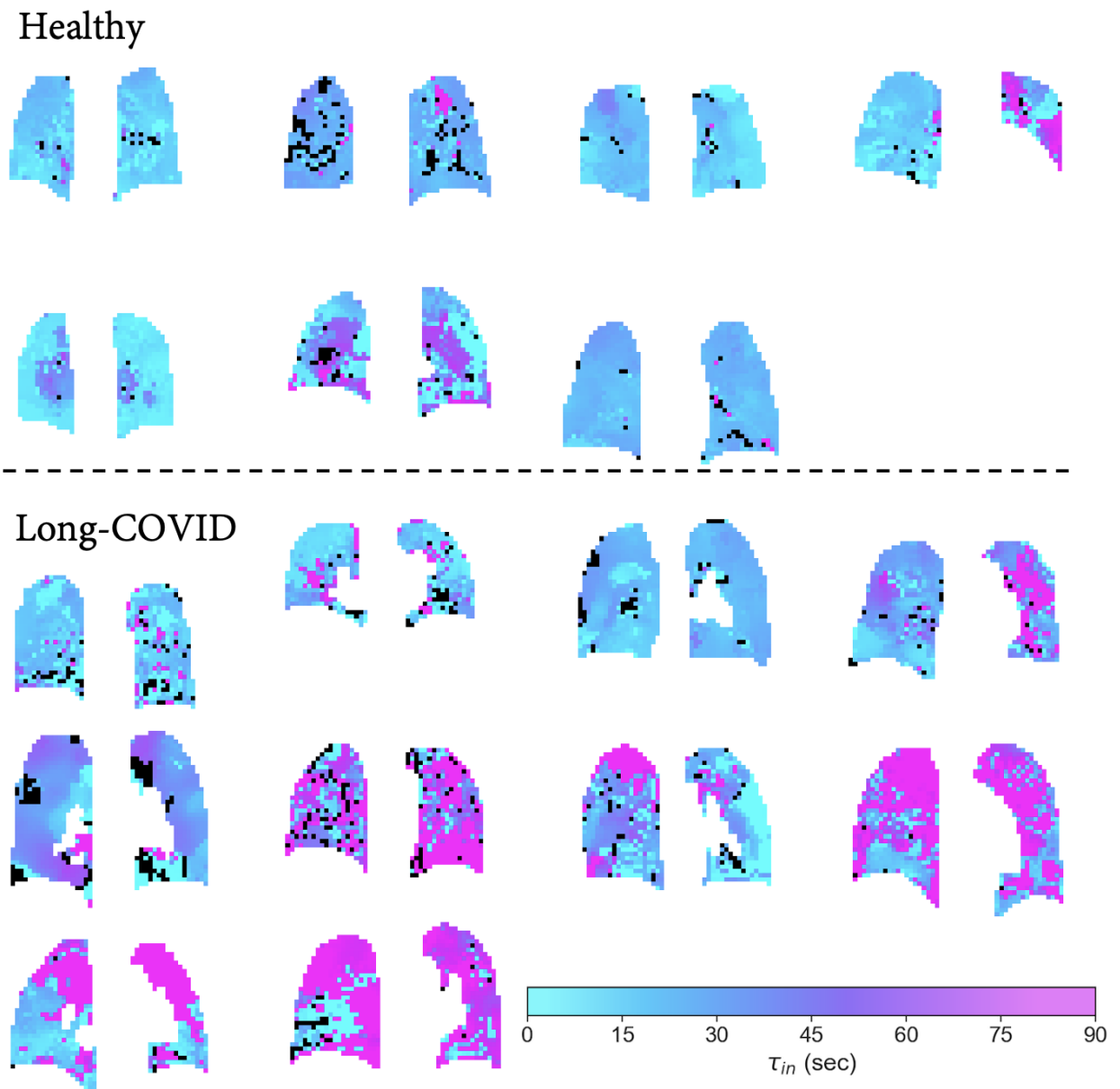


Figure 4.11: Fitted wash-in rate τ_{in} in third coronal slice for estimated oxygen responses from ICA Algorithm 3. Black pixels represent voxels where models f_5 or f_6 provided the best fit (i.e. not oxygen-activated).

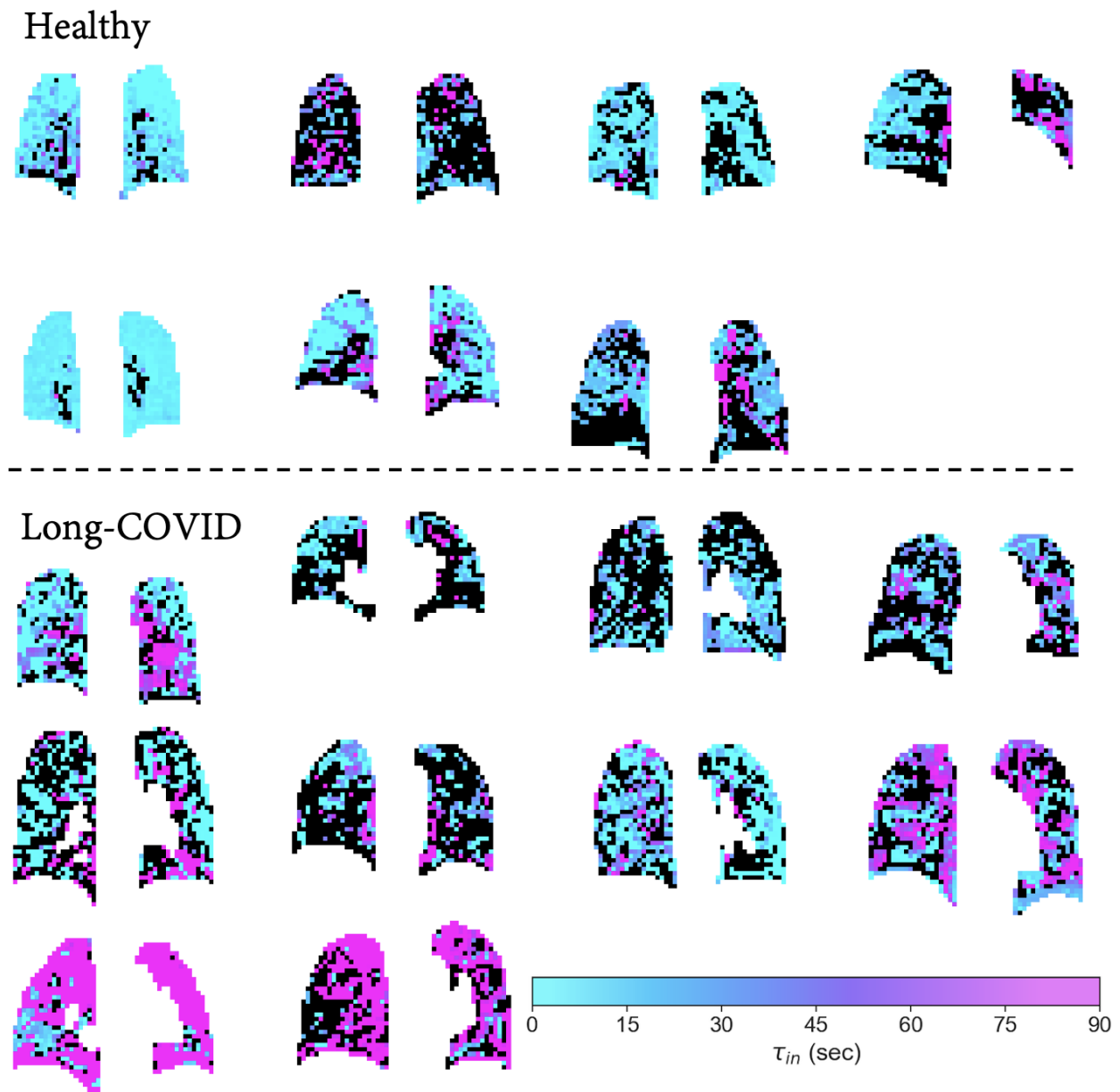


Figure 4.12: Fitted wash-in rate τ_{in} in third coronal slice for raw time series. Black pixels represent voxels where models f_5 or f_6 provided the best fit (i.e. not oxygen-activated).

To achieve a more fair comparison, we therefore re-run the above bootstrap tests using only voxels that were oxygen activated when both the raw time series and the estimated OE response from 3 were used. Table 4.3 shows the corresponding results.

Data / Param.	τ_{in}	τ_{out}	Δt	$ \Delta S $	\bar{R}
ICA	[3.39, 19.46]*	[1.14, 13.73]*	[-1.81, 17.62]	[-0.31, 1.78]	[-0.23, -0.07]*
Raw	[-0.42, 20.65]	[-1.05, 19.09]	[6.06, 22.99]*	[-0.91, 3.89]	[-0.03, 0.03]

Table 4.3: Bootstrapped parameters CIs for $\mathbb{E}[\mu | \text{COVID}] - \mathbb{E}[\mu | \text{Healthy}]$ only in voxels deemed oxygen-activated when fitted using both the raw time series and the estimated oxygen responses using Algorithm 3. An asterisk denotes that we reject the null hypothesis of no significant difference at the 5% significance level.

4.5 Discussion

Using the cohort-level mean of means as a distribution-level effect size, we did not find evidence of a difference in voxel-wise oxygen-response weights between cohorts. Consistently, neither analysis revealed a significant difference in the magnitude parameter $|\Delta S|$. The implication is that the oxygen response (of oxygen activated voxels) explains similar amounts of variance in the healthy and long COVID cohorts. Note that the quantity \bar{a}_v^2 is closely related to the quantity $|\Delta S|$ in each oxygen activated voxel since the extracted oxygen component is a weighted sum of unit variance, zero mean time series; the weights being the loadings $(a_v^{\text{OE}})_k$ whose squared sum is proportional to \bar{a}_v^2 . According to models $f_1 - f_4$, $2\Delta S$ represents the magnitude of the oxygen response in a particular voxel. It should be noted that in the case of the raw data, $2\Delta S$ takes the same units as voxel intensity. In the case of the ICA data, $2\Delta S$ has units of equal to those of the loadings $(a_v^{\text{OE}})_k$, which may be interpreted as roots of the variance contribution from the estimated oxygen response. It may have been better to express ΔS as a percent signal enhancement (PSE) relative to the baseline for fits for both the raw- and ICA data. Such a quantity may have been more pertinent for comparison of cohorts. However, the focus of this text was on varying shapes in the oxygen response, rather than the magnitude of the response.

It is not surprising that a higher proportion of voxels is found to be oxygen-activated when fitting to the extracted oxygen component from the ICA algorithm (Algorithm 3) as opposed to the raw time series. The reason is that we actively look for independent components which are maximally periodic at a particular frequency. However, the fact that no significant difference may be found between the proportion of oxygen-activated voxels of the cohorts is surprising as it indicates that similar proportions of the lungs react to the gas switching scheme in both cohorts.

The statistically significant differences in wash-in and wash-out times between cohorts established by the present method shows that it is sensitive to disease status. More importantly, the large fraction of voxels that are deemed oxygen activated, compared with fits to the raw time series, indicates that the present method is more sensitive to changes induced by the cyclic inhalation of oxygen. No significant difference was found for the wash-out rates when models were fitted to the raw time series. Because activation rates differed (ICA ~96%/92% vs raw 66%/58%), we repeated the comparison on voxels activated by both methods (Table 4.3) to ensure a fairer like-for-like assessment; conclusions were unchanged for the data from Algorithm 3, whereas the difference in wash-in rates for the raw time series were no longer statistically significant. This shows that the present method yields similar results even when truncated to a smaller proportion of voxels.

It should be noted that the upper bound of 90 seconds for the wash-in and wash-out parameters may have contributed to these findings as a non-zero proportion of voxels reached this upper bound (see figures 4.6 and 4.7). The majority of voxels reaching this threshold are from subjects with long COVID. Allowing higher values in those voxels may induce further statistically significant differences in the wash-in/wash-out rates of the raw fits. It should also be noted that model f_3 gave the best AICc score in a significant proportion of voxels when considering the estimated oxygen responses from Algorithm 3. Since we set $\tau_{\text{in}} = \tau_{\text{out}}$ in those voxels, it follows that the differences between cohorts in one parameter are not surprising given differences in the other.

No statistical significance was found in oxygen-activated voxels for the oxygen

response delay Δt when fitting on the data from Algorithm 3. Such a difference *was* found in the identified oxygen-activated voxels using the raw fits. It is possible that this difference is due to the reduction in reference functions which was used in the implementation of Algorithm 3. In particular, it is possible that reducing the number of reference functions resulted in the "wrong" component being selected in some instances, likely when the best components from different dimensionalities c had similar degrees of periodicity. To alleviate this issue, it would be possible to identify the most periodic component instead by Fourier decomposition. Due to the limited number of gas switching cycles, however, this may not always be an attractive option. Again, we note from figure 4.8 that for both data sources, some proportion of voxels reach the maximal delay of 90 seconds in the oxygen response. However, this proportion is similar across cohorts. Testing for delays $\Delta t \geq 60$ is possible and may reveal statistically significant differences for the ICA data, but as mentioned, it may make for problems of identifying which gas switch a time series is responding to.

Finally, we find a statistically significant difference for the adjusted coefficient of determination \bar{R}^2 using Algorithm 3 which is not present in the raw data (see Figure 4.10). This suggests that the oxygen response in diseased cohorts follow different reference functions to those in healthy cohorts, despite showing similar magnitudes of the oxygen response.

Chapter 5

General Conclusions and Future Work

In this work, we have developed an algorithm using temporal ICA to extract spatially varying estimates of the response to gas switching in the lungs during oxygen-enhanced MRI scans. Fitting the estimated response in each voxel from such an MRI scan to a set of reference functions, we find that the method leads to statistically significant differences in the estimated wash-in and wash-out rates between a cohort of healthy subjects and a cohort of subjects with long COVID. In addition to the fact that no such differences were found using the raw time series of each voxel, the present method greatly increases, relative to raw time series, the proportion of voxels in which a periodic, gas-sensitive reference function makes for a better fit than a constant or linear function (from $\sim 60\%$ to $> 90\%$). Consequently, the promise of the present method is as a tool which can be used to spot changes in gas sensitivity in a spatially resolved manner which may be indicative of early disease status. However, the ICA algorithm presented here was not able to identify significant differences between cohorts in terms of the gas switching response delay Δt . Such a difference was present when fitting to the raw time series, and this indicates that the present method would likely be best used in combination with analysis of the raw time series and existing methods such as the lung-wide temporal ICA applied in [5].

Future extensions of the present work should likely fit the wash-in/wash-out

and delay parameters $\tau_{\text{in}}, \tau_{\text{out}}, \Delta t$ without the upper bound of 90 seconds. Furthermore, it is possible that computational times could be further reduced by defining upper thresholds on the explained variance proportion in the whitened data \mathbf{Z} when doing ICA in each window $W(a; r)$. This would allow further restrictions on dimensionality c to be tested in each window. It would also be beneficial to do further investigations on differences in oxygen response between slices in the same subjects and across cohorts. Finally, future work should use both echoes from the sequence proposed by [15] and apply Algorithm 3 to the estimated relaxation rate T_2^* in each voxel. This would allow isolation of the changes due to increased susceptibility gradients at the gas-tissue interface from changes such as T_1 reduction in blood and potential vasodilation.

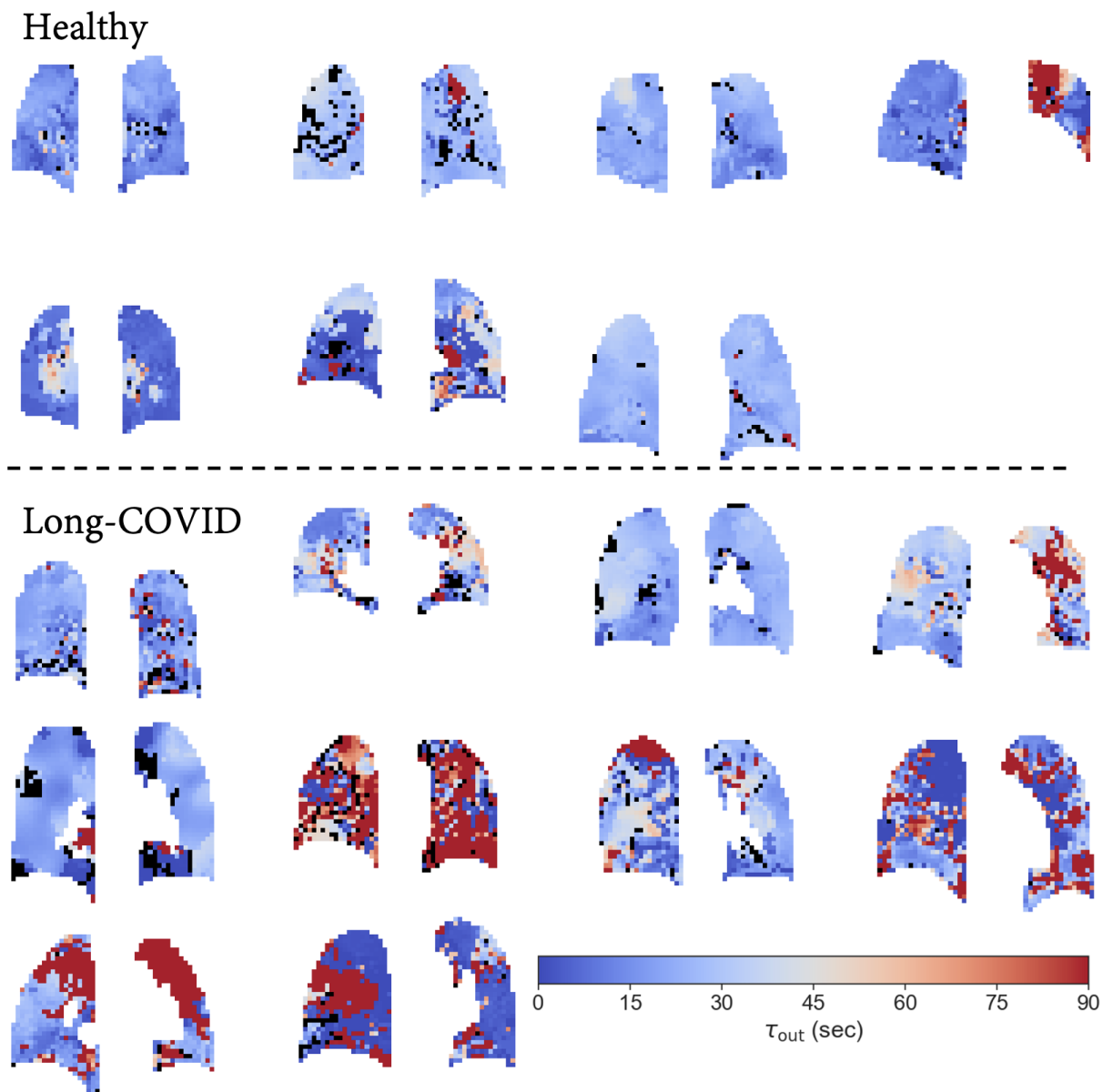
A Further Parameter Maps

Figure 1: Fitted wash-out rate τ_{out} in third coronal slice for estimated oxygen responses from ICA Algorithm 3. Black pixels represent voxels where models f_5 or f_6 provided the best fit (i.e. not oxygen-activated).

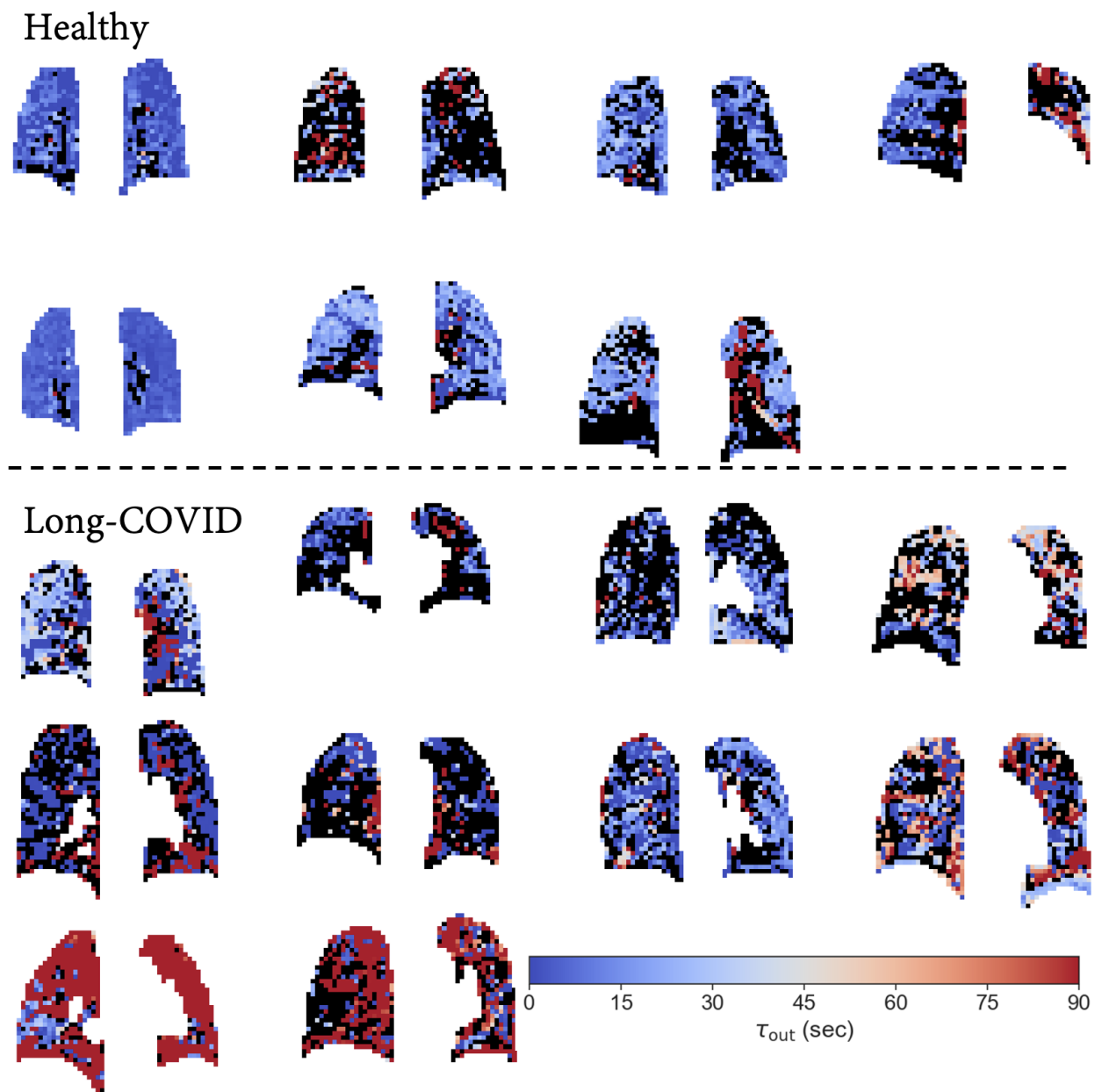


Figure 2: Fitted wash-out rate τ_{out} in third coronal slice for raw time series. Black pixels represent voxels where models f_5 or f_6 provided the best fit (i.e. not oxygen-activated).

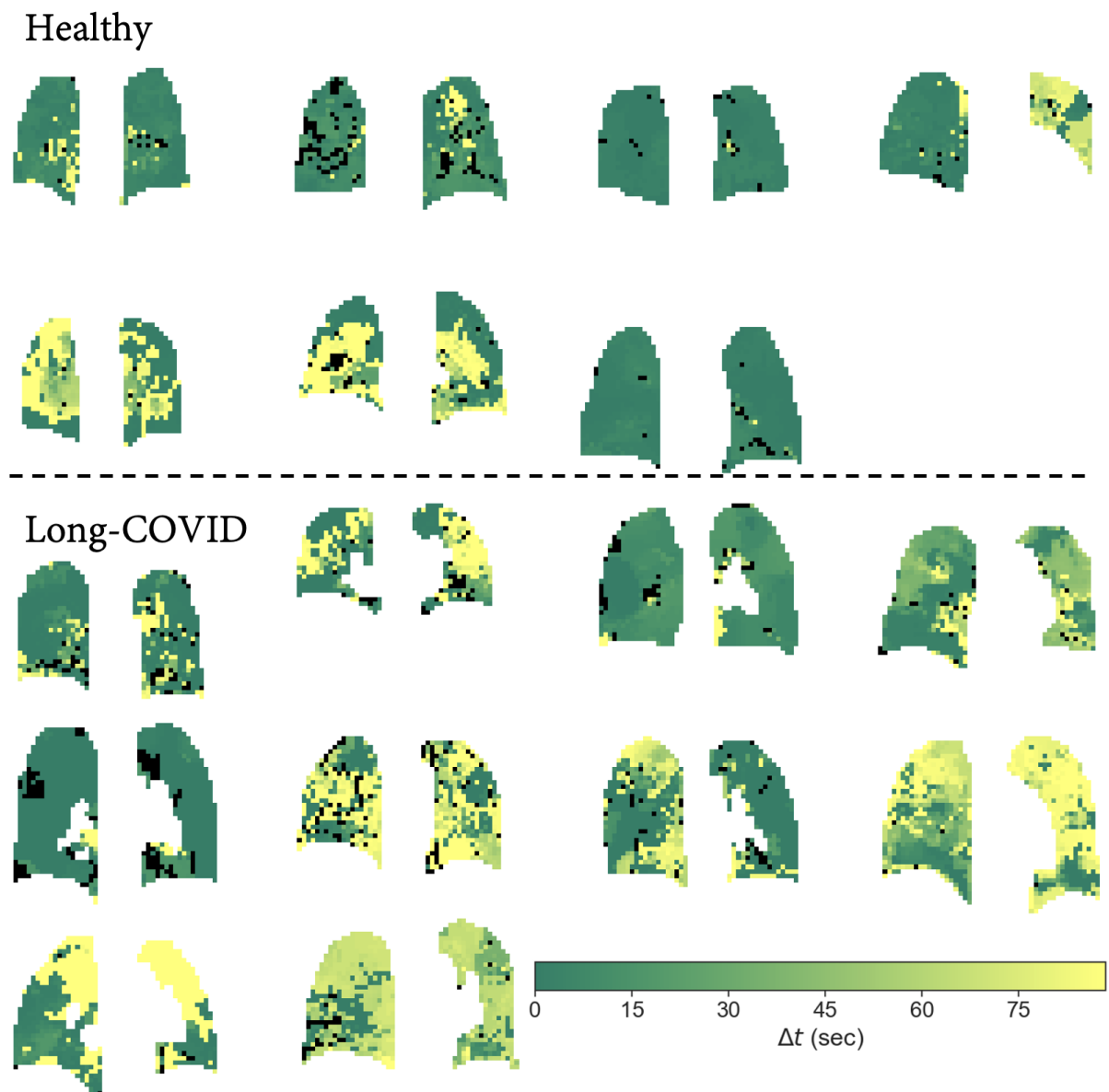


Figure 3: Fitted delay Δt in third coronal slice for estimated oxygen responses from ICA Algorithm 3. Black pixels represent voxels where models f_5 or f_6 provided the best fit (i.e. not oxygen-activated).

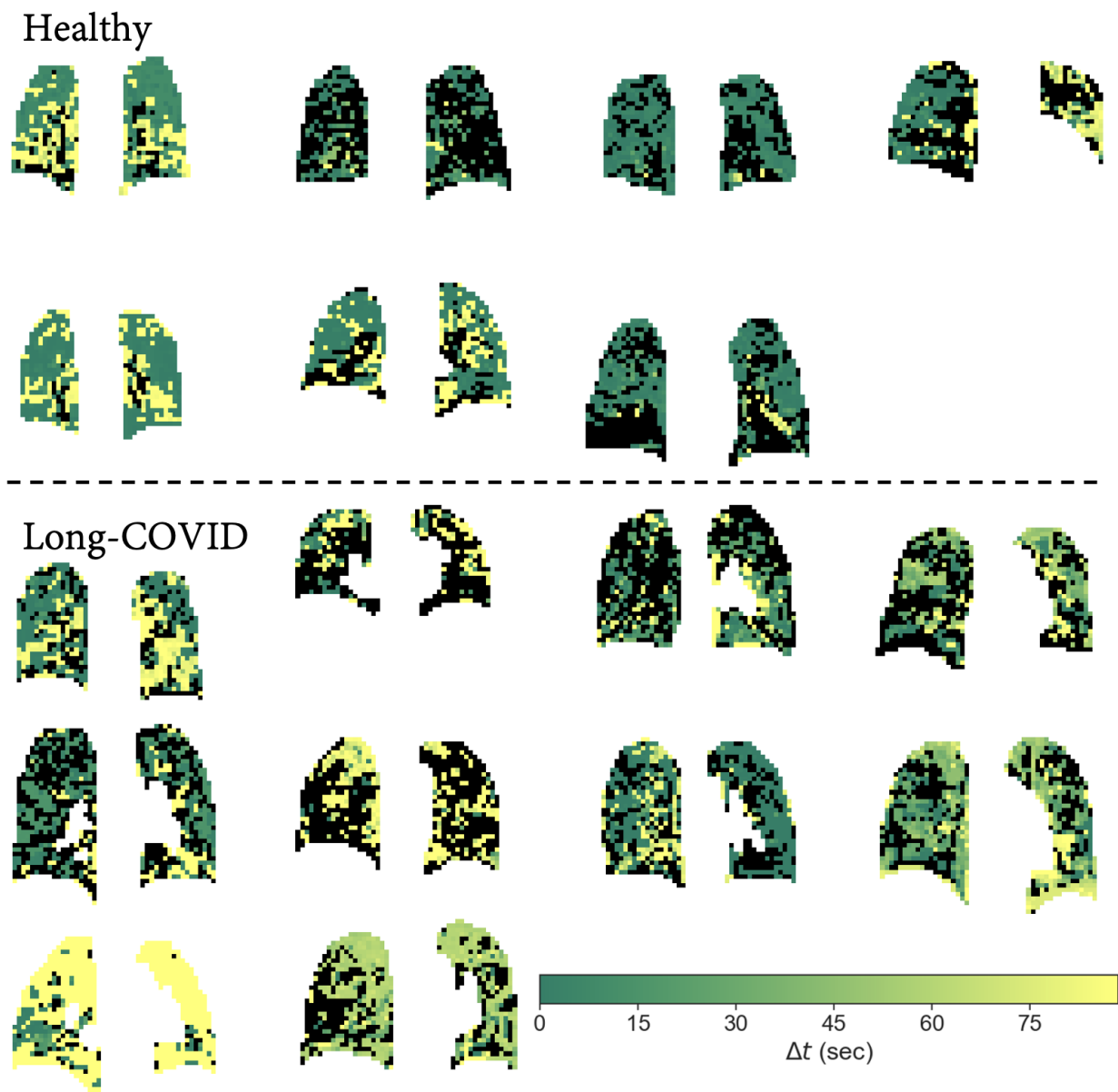


Figure 4: Fitted delay Δt in third coronal slice for estimated oxygen responses from ICA Algorithm 3. Black pixels represent voxels where models f_5 or f_6 provided the best fit (i.e. not oxygen-activated).

Bibliography

- [1] Xiang Kong, Hui Xue Sheng, Guang Ming Lu, Felix G. Meinel, Kevin T. Dyer, U. Joseph Schoepf, and Long Jiang Zhang. Xenon-enhanced dual-energy ct lung ventilation imaging: Techniques and clinical applications. *American Journal of Roentgenology*, 202(2):309–317, 2014. PMID: 24450670.
- [2] Agilo L. Kern, Filip Klimeš, Andreas Voskrebenev, Hoen-Oh Shin, and Jens Vogel-Claussen. Functional pulmonary imaging. *Journal of Magnetic Resonance Imaging*, n/a(n/a):1–23, 2025.
- [3] S. Sivaram Kaushik, Scott H. Robertson, Matthew S. Freeman, Mu He, Kevin T. Kelly, Justus E. Roos, Craig R. Rackley, W. Michael Foster, H. Page McAdams, and Bastiaan Driehuys. Single-breath clinical imaging of hyperpolarized ^{129}Xe in the airspaces, barrier, and red blood cells using an interleaved 3d radial 1-point dixon acquisition. *Magnetic Resonance in Medicine*, 75(4):1434–1443, 2016.
- [4] Olaf Dietrich, Ulrike I. Attenberger, Michael Ingrisch, Daniel Maxien, Michael Peller, Konstantin Nikolaou, and Maximilian F. Reiser. Analysis of signal dynamics in oxygen-enhanced magnetic resonance imaging. *Investigative Radiology*, 45(4):165–173, 2010.
- [5] Sarah H. Needleman, Mina Kim, Jamie R. McClelland, Josephine H. Naish, Marta Tibiletti, James P. B. O’Connor, and Geoff J. M. Parker. Independent component analysis (ica) applied to dynamic oxygen-enhanced mri (oe-mri) for robust functional lung imaging at 3t. *Magnetic Resonance in Medicine*, 91(3):955–971, 2024.

- [6] Hidetoshi Nakamura, Toyohiro Hirai, Hajime Kurosawa, Kazuki Hamada, Kazuto Matsunaga, Kaoruko Shimizu, Satoshi Konno, Shigeo Muro, Koichi Fukunaga, Yasutaka Nakano, Ichiro Kuwahira, and Masayuki Hanaoka. Current advances in pulmonary functional imaging. *Respiratory Investigation*, 62(1):49–65, 2024. Available online 8 November 2023.
- [7] Dipan Karmali, Mudiaga Sowho, Sonali Bose, Jackson Pearce, Vickram Tejwani, Zuzana Diamant, Keerthi Yarlagadda, Erick Ponce, Nina Eikelis, Tamas Otvos, Akram Khan, Michael Lester, Andreas Fouras, Jason Kirkness, and Trishul Siddharthan. Functional imaging for assessing regional lung ventilation in preclinical and clinical research. *Frontiers in Medicine*, 10:1160292, 2023.
- [8] Sam Bayat, Jim Wild, and Tilo Winkler. Lung functional imaging. *Breathe*, 19(3), 2023.
- [9] Simon M.F. Triphan, Grzegorz Bauman, Philip Konietzke, Marilisa Konietzke, Mark O. Wielpütz, and the International Workshop for Pulmonary Functional Imaging (IWPFI). Magnetic resonance imaging of lung perfusion. *Journal of Magnetic Resonance Imaging*, 59(3):784–796, 2024.
- [10] Andreas Voskrebenev, Marcel Gutberlet, Filip Klimeš, Till F. Kaireit, Christian Schönenfeld, Alexander Rotärmel, Frank Wacker, and Jens Vogel-Claussen. Feasibility of quantitative regional ventilation and perfusion mapping with phase-resolved functional lung (preful) mri in healthy volunteers and copd, cteph, and cf patients. *Magnetic Resonance in Medicine*, 79(4):2306–2314, 2018.
- [11] Robert R. Edelman, Hiroto Hatabu, Eiji Tadamura, Wei Li, and Potthumarthi V. Prasad. Noninvasive assessment of regional ventilation in the human lung using oxygen-enhanced magnetic resonance imaging. *Nature Medicine*, 2(11):1236–1239, 1996.

- [12] Pengfei Xu, Thomas Meersmann, Jing Wang, and Chengbo Wang. Review of oxygen-enhanced lung mri: Pulse sequences for image acquisition and t1 measurement. *Medical Physics*, 50(10):5987–6007, 2023.
- [13] Vu M. Mai, Qun Chen, Alexander A. Bankier, and Robert R. Edelman. Multiple inversion-recovery mr subtraction imaging of human ventilation from inhalation of room air and pure oxygen. *Magnetic Resonance in Medicine*, 43(6):913–916, 2000.
- [14] Simon M.F. Triphan, Felix A. Breuer, Daniel Gensler, Hans-Ulrich Kauczor, and Peter M. Jakob. Oxygen enhanced lung mri by simultaneous measurement of t1 and t2* during free breathing using ultrashort te. *Journal of Magnetic Resonance Imaging*, 41(6):1708–1714, 2015.
- [15] Mina Kim, Josephine H. Naish, Sarah H. Needleman, Marta Tibiletti, Yohn Taylor, James P. B. O'Connor, and Geoff J. M. Parker. Feasibility of dynamic t2*-based oxygen-enhanced lung mri at 3t. *Magnetic Resonance in Medicine*, 91(3):972–986, 2024.
- [16] Yoshiharu Ohno, Hisanobu Koyama, Munenobu Nogami, Daisuke Takenaka, Sumiaki Matsumoto, Makoto Obara, and Kazuro Sugimura. Dynamic oxygen-enhanced mri versus quantitative ct: Pulmonary functional loss assessment and clinical stage classification of smoking-related copd. *American Journal of Roentgenology*, 190(2):W93–W99, 2008. PMID: 18212207.
- [17] Josephine H. Naish, Geoffrey J. M. Parker, Paul C. Beatty, Alan Jackson, Simon S. Young, John C. Waterton, and Chris J. Taylor. Improved quantitative dynamic regional oxygen-enhanced pulmonary imaging using image registration. *Magnetic Resonance in Medicine*, 54:464–469, 2005.
- [18] Hiroto Hatabu, Eiji Tadamura, Qun Chen, Klaus W. Stock, Wei Li, Potumarthi V. Prasad, and Robert R. Edelman. Pulmonary ventilation: dynamic mri with inhalation of molecular oxygen. *European Journal of Radiology*, 37:172–178, 2001.

- [19] Marta Tibiletti, James A. Eaden, Josephine H. Naish, Paul J.C. Hughes, John C. Waterton, Matthew J. Heaton, Nazia Chaudhuri, Sarah Skeoch, Ian N. Bruce, Stephen Bianchi, Jim M. Wild, and Geoff J.M. Parker. Imaging biomarkers of lung ventilation in interstitial lung disease from ^{129}Xe and oxygen enhanced 1h mri. *Magnetic Resonance Imaging*, 95:39–49, 2023.
- [20] Aapo Hyvärinen and Erkki Oja. Independent component analysis: algorithms and applications. *Neural Networks*, 13(4):411–430, 2000.
- [21] scikit-learn development team. *sklearn.decomposition.FastICA — scikit-learn 1.7.1 documentation*. scikit-learn, 2025. Version 1.7.1, released July 2025. Accessed 3 May 2025.
- [22] Aapo Hyvärinen, Juha Karhunen, and Erkki. Oja. *Independent component analysis*. Adaptive and learning systems for signal processing, communications, and control. Wiley, New York ;, 2001.
- [23] J. Himberg and A. Hyvarinen. Icasso: software for investigating the reliability of ica estimates by clustering and visualization. In *2003 IEEE XIII Workshop on Neural Networks for Signal Processing (IEEE Cat. No.03TH8718)*, pages 259–268, 2003.
- [24] A. M. Kagan, Yuri Linnik, C. R. Rao, and Balasubrahmanyan. Ramachandran. *Characterization problems in mathematical statistics - translated from Russian text by B. Ramachandran*. Wiley series in probability and mathematical statistics. Wiley-Interscience, New York ;, 1973.
- [25] Olivier Rioul. Optimal transport to the entropy-power inequality and a reverse inequality. *CoRR*, abs/1701.08534, 2017.
- [26] Scott Makeig, Sigurd Enghoff, Tzzy-Ping Jung, and Terrence J. Sejnowski. Moving-window ica decomposition of eeg data reveals event-related changes in oscillatory brain activity. In *Second International Workshop on Independent Component Analysis and Signal Separation, June 19-22, Helsinki, Finland*, 2000.

- [27] Fabrizio Esposito, Erich Seifritz, Elia Formisano, Renato Morrone, Tommaso Scarabino, Gioacchino Tedeschi, Sossio Cirillo, Rainer Goebel, and Francesco Di Salle. Real-time independent component analysis of fmri time-series. *NeuroImage*, 20(4):2209–2224, 2003.
- [28] Vesa Kiviniemi, Tapani Vire, Jukka Remes, Ahmed Abou Elseoud, Tuomo Starck, Osmo Tervonen, and Juha Nikkinen. A sliding time-window ica reveals spatial variability of the default mode network in time. *Brain Connectivity*, 1(4):339–347, 2011. PMID: 22432423.
- [29] Elena A. Allen, Eswar Damaraju, Sergey M. Plis, Erik B. Erhardt, Tom Eichele, and Vince D. Calhoun. Tracking whole-brain connectivity dynamics in the resting state. *Cerebral Cortex*, 24(3):663–676, 11 2012.